1 **Mitophagy antagonism by Zika virus reveals Ajuba as a regulator of PINK1-Parkin signaling,**

2 **PKR-dependent inflammation, and viral invasion of tissues.**

3

4

5 Sanket S. Ponia[1], Shelly J. Robertson[1], Kristin L. McNally[1], Gail L. Sturdevant[1], Matthew Lewis[1],

6 Forrest Jessop[2], Catherine M. Bosio[2], Catherine Kendall[1,3], Dylan Gallegos[1], Arielle Hay[1], Cindi

7 Schwartz[4], Rebecca Rosenke[5], Greg Saturday[5], Craig Martens[4], and Sonja M. Best[1*]

8

9 [1]Innate Immunity and Pathogenesis Section, Laboratory of Virology, Rocky Mountain

10 Laboratories, National Institute of Allergy and Infectious Diseases, NIH, Hamilton, MT 59840.

11 [2]Immunity to Pulmonary Pathogens Section, Laboratory of Bacteriology, Rocky Mountain

12 Laboratories, National Institute of Allergy and Infectious Diseases, NIH, Hamilton, MT 59840.

13 [3]School of Molecular and Cellular Biology, University of Leeds, Leeds, United Kingdom.

14 [4]Research Technology Branch, Rocky Mountain Laboratories, National Institute of Allergy and

15 Infectious Diseases, NIH, Hamilton, MT 59840.

16 [5]Rocky Mountain Veterinary Branch, Rocky Mountain Laboratories, National Institute of Allergy

17 and Infectious Diseases, NIH, Hamilton, MT 59840.

18

19 *Corresponding and lead author: sbest@niaid.nih.gov

20

21

22

23

24

25

26

27

28

29

ABSTRACT

Dysregulated inflammation dominated by chemokine expression is a key feature of disease following infection with the globally important human pathogens, Zika virus (ZIKV) and dengue virus, but a mechanistic understanding of how pro-inflammatory responses are initiated is lacking. Mitophagy is a quality control mechanism that regulates innate immune signaling and cytokine production through selective degradation of damaged mitochondria. Here, we demonstrate that ZIKV NS5 antagonizes mitophagy by binding to the host protein Ajuba and preventing its translocation to depolarized mitochondria where it is required for PINK1 activation and downstream signaling. Consequent mitophagy suppression amplified the production of pro-inflammatory chemokines through PKR sensing of mitochondrial RNA. In Ajuba$^{-/-}$ mice, ZIKV induced early expression of pro-inflammatory chemokines associated with significantly enhanced dissemination to tissues. This work identifies Ajuba as a critical regulator of mitophagy, and demonstrates a role for mitophagy in limiting systemic inflammation following infection by globally important human viruses.

INTRODUCTION

Zika virus (ZIKV), a mosquito-borne flavivirus, was first isolated in Uganda (1957) but underwent an explosive emergence first affecting pacific islanders of Yap (2007) and French Polynesia (2013), before being introduced into the Americas via Brazil (2014). Although approximately 80% of infections in adults are asymptomatic or mild, infection can cause the neurological disorder Guillain-Barré syndrome or result in severe congenital neurological sequelae during pregnancy (Pierson and Diamond, 2020). Serum biomarkers of acute phase immune responses are dominated by chemokines that become highly elevated in severe disease (Foo et al., 2018; Kam et al., 2017; Michlmayr et al., 2017; Michlmayr et al., 2020; Naveca et al., 2018). Chemokine and other pro-inflammatory responses are critical in leucocyte recruitment and control of virus infection, although uncontrolled or excessive inflammatory responses are drivers of immunopathology (Melchjorsen et al., 2003). Therefore, determining the innate

59   immune signaling mechanisms that drive pro-inflammatory chemokine expression following

60   flavivirus infection is key to understanding flavivirus pathogenesis and development of

61   therapeutics.

62

63   Mitochondria are critical to the coordination of interferon (IFN) and inflammatory responses to

64   infection with RNA viruses through two major mechanisms. The first is as a membrane platform

65   to relay initial detection of viral double stranded RNA (dsRNA) by the RIG-I-like helicases (RLR),

66   RIG-I and Mda5. Downstream signal transduction requires mitochondrial antiviral signaling

67   protein (MAVS) on the surface of mitochondria to coordinate the transcriptional activation of

68   type I and III IFNs (Mills et al., 2017). The second role of mitochondria is through release of

69   danger associated molecular patterns (DAMPs) (West et al., 2015) including mitochondrial DNA,

70   RNA, and cardiolipin. These signal through various pattern-recognition receptors (PRRs)

71   including cGAS-STING, Mda5, protein kinase R (PKR), and the inflammasome (Youle, 2019). Both

72   RLR- and DAMP-dependent responses are regulated by dynamic remodeling of the

73   mitochondrial network including fusion to form elongated networks, fission to fragment

74   mitochondria, and mitophagy to selectively remove irreparably damaged mitochondria through

75   autophagolysosomal degradation (Harper et al., 2018). Failure to eliminate damaged

76   mitochondria drives chronic inflammation that is linked to the neurodegenerative diseases such

77   as Parkinson's disease (PD) and Alzheimer's disease (AD) (Mottis et al., 2019; Sliter et al., 2018).

78

79   The most well characterized pathway of mitophagy is governed by two genes, the kinase PTEN-

80   induced putative kinase 1 (*PINK1*) and the E3 ubiquitin ligase Parkin (*PRKN*), that are mutated in

81   familial forms of PD (Harper et al., 2018; Sekine and Youle, 2018). Following loss of

82   mitochondrial potential, PINK1 accumulates on the surface of depolarized mitochondria where

83   it activates itself through phosphorylation and then phosphorylates ubiquitin (Ub) on Ser65

84   (pS65-Ub). pS65-Ub recruits and retains Parkin at the mitochondria, enabling Parkin to be

85   phosphorylated and activated by PINK1. Parkin then works cooperatively with PINK1 to build

86   pS65-Ub chains on mitochondrial outer membrane proteins and recruit the

87   autophagolysosomal machinery that ultimately results in mitochondrial clearance (reviewed in

88   (Harper et al., 2018; Sekine and Youle, 2018)). In the context of RLR signaling, MAVS activation

89   results in oxidative damage that triggers mitophagy as one mechanism to resolve this response

90   (Song et al., 2020). To date, viruses have only been shown to increase mitophagy in order to

91   dampen RLR signaling. However, while examples of viruses that inhibit mitophagy are not

92   known, retention of damaged mitochondria in infected cells may have major implications to the

93   host inflammatory response.

94

95   Here we reveal that ZIKV antagonizes PINK1-Parkin signaling to suppress mitophagy and that

96   this is directly translated to pro-inflammatory chemokine expression through PKR. We show

97   that the flavivirus nonstructural protein 5 (NS5) interacts with the cellular protein Ajuba to

98   suppress PINK1-Parkin dependent mitophagy. Ajuba belongs to the LIM family of proteins

99   whose demonstrated functions include the relief of Ser/Thr kinase autoinhibition and as

100   scaffolding adaptor proteins to promote association of multi-protein complexes (Jia et al.,

101   2020). Ajuba has been identified as an activator of mitotic kinases, including Aurora-A and CDK1

102   (Chen et al., 2016; Hirota et al., 2003), that also have central functions in mitochondrial

103   dynamics (Archer, 2013). Our results demonstrate that Ajuba is recruited to mitochondria

104   following various inducers of mitochondrial stress including MAVS activation where it is

105   required for efficient activation of PINK1. The consequences of mitophagy antagonism to ZIKV

106   infection include increased induction of pro-inflammatory chemokines considered to be

107   biomarkers of ZIKV disease severity in humans. We also show that these chemokine responses

108   are PKR-dependent, the activation of which occurs in response to increased release of

109   mitochondrial RNA (mtRNA). Finally, we show that suppressed mitophagy results in earlier

110   amplification of inflammatory responses in response to ZIKV infection in mice, and facilitates

111   increased viral invasion of tissues. Together, this work identifies Ajuba as a critical regulator of

112   mitophagy and demonstrates a systemic role of mitophagy in limiting inflammation and

113   protection from globally important human viruses in vivo.

114

115

116

117   **RESULTS**

118

119   **Ajuba negatively regulates MAVS expression dependent on mitophagy.**

120   An interaction between Ajuba and the NS5 proteins of flaviviruses was implicated from a yeast

121   2-hybrid performed using a cDNA library from mouse macrophages (Taylor et al., 2011) (this

122   aspect is experimentally addressed in Figure 4B). As ZIKV NS5 is multifunctional protein with

123   central roles in antagonism of host IFN responses (Grant et al., 2016; Xia et al., 2018), we first

124   examined the potential of Ajuba to regulate RLR-MAVS signaling (Stone et al., 2019; Suthar et

125   al., 2013). IFNβ expression can be induced through this pathway in tissue culture by

126   overexpression of MAVS. *IFNB* mRNA driven by MAVS was reduced by ~84% in the presence of

127   Ajuba (Figure 1A) and was associated with reduced MAVS expression (Figure 1B). Expression of

128   a related LIM family member, LIMD1, had similar but less pronounced effects on expression of

129   both MAVS and *IFNB* mRNA, suggesting that members of the LIM family may redundantly

130   regulate RLR signaling at the level of MAVS. Replication of vesicular stomatitis virus (VSV), often

131   used as a biological indicator of IFN sensitivity, was lower in human A549 cells depleted for

132   *AJUBA* or *LIMD1* mRNA expression by siRNAs consistent with a role for Ajuba in negative

133   regulation of RLR signaling (Supplemental Figure 1). We also observed recruitment of Ajuba to

134   mitochondria following infection with Sendai virus (Figure 1E), a virus used to trigger the RLR-

135   MAVS pathway. However, we did not observe an interaction between Ajuba and MAVS by

136   immunoprecipitation (IP) (data not shown), suggesting that a role for Ajuba may be indirect.

137   Indeed, ectopic expression of Ajuba in HEK293T cells also reduced the endogenous expression

138   of an additional integral mitochondrial protein, TIMM44. Ajuba-induced loss of both MAVS and

139   TIMM44 was recovered in the presence of either bafilomycin A1 (BafA1) or epoxomicin,

140   inhibitors of lysosome- and proteasome-dependent degradation, respectively (Figure 1D). The

141   major pathway that utilizes both of these cellular degradation pathways is mitophagy. Here, the

142   proteasome degrades outer membrane mitochondrial proteins ubiquitinated by Parkin,

143   whereas lysosomes fused to autophagosomes ultimately degrade damaged mitochondria

144   (Harper et al., 2018; Sekine and Youle, 2018). Consistent with a role in mitophagy, Ajuba

145   expression did not alter MAVS expression in HeLa cells that are naturally deficient in Parkin

5

146   (Heo et al., 2015; Ordureau et al., 2014). MAVS degradation was restored following expression

147   of wild-type Parkin, but not the C431F active site mutant (Figure 1E). As MAVS signaling is

148   negatively regulated by mitophagy (He et al., 2019; Yang et al., 2018), these results raise the

149   possibility that Ajuba regulates mitophagy more generally rather than having a specific role in

150   RLR-MAVS antiviral responses.

151

152   **Ajuba is regulated by PINK1-Parkin-mediated degradation during mitophagy.**

153   To determine if Ajuba responds generally to mitochondrial damage, mitophagy competent

154   HEK293T cells expressing Ajuba were treated with carbonyl cyanide m-chlorophenyl hydrazone

155   (CCCP) that acts as a proton ionophore to depolarize mitochondrial membrane potential

156   (Fujimaki et al., 2018). CCCP treatment induced translocation of Ajuba from the cytosol to

157   mitochondria-enriched fractions in less than 30 min post treatment (Figure 2A). Similar to

158   overexpression of MAVS, treatment of cells with additional inducers of oxidative stress,

159   tunicamycin and oligomycin, also resulted in reduced expression of integral mitochondrial

160   proteins Mfn1 and TIMM44 in the presence of Ajuba, but not the ER-resident calreticulin

161   (Figure 2B). This suggests that Ajuba responds generally to oxidative stress to specifically

162   promote mitochondrial degradation. In Figures 1E and 2B, we also observed reduced

163   expression of Ajuba when mitophagy was induced for periods longer than 6 h. To examine this

164   more closely, HEK293T cells expressing Ajuba were treated with CCCP or starved to induce bulk

165   autophagy for 6 h and treated with inhibitors of degradation. The CCCP-induced reduction of

166   Ajuba and Mfn1 was dependent on both lysosome- and proteasome-mediated degradation.

167   However, expression of Ajuba or Mfn1 was not responsive to bulk autophagy as evidenced by

168   starvation-induced degradation of the ER-resident autophagy receptor, FAM134B (Khaminets et

169   al., 2015) that is rescued by lysosome inhibition only (Figure 2C). Thus, Ajuba responds

170   specifically to mitochondrial damage. To determine if Ajuba degradation during mitophagy was

171   dependent on PINK1 or Parkin, Ajuba was expressed in the well-established HeLa cell model

172   lacking either protein (Heo et al., 2015). Both basal expression and CCCP-dependent

173   degradation of Ajuba were dependent on PINK1 and Parkin, with Ajuba degradation responding

174   to CCCP and the presence of PINK1 or Parkin in a manner similar to Mfn1 (Figure 2D). To

6

175   determine if Ajuba has a role in mitochondrial function, we generated an Ajuba$^{-/-}$ mouse model

176   (Supplementary Figure 2), and measured oxygen consumption rates (OCR) by Seahorse

177   Bioanalyzer assays in age-matched WT, Ajuba$^{-/-}$ or PINK1$^{-/-}$ mouse embryonic fibroblasts (MEFs)

178   (Figure 2E, F). Measures of basal respiration ATP-linked respiration, proton leak, spare

179   respiratory capacity and non-mitochondrial respiration were similar between the three MEF

180   genotypes. However, Ajuba$^{-/-}$ MEFs demonstrated increased maximal respiration, thereby

181   confirming that Ajuba regulates mitochondrial function. Taken together, these results suggest

182   that Ajuba responds to a variety of mitochondrial stressors by translocating to mitochondria,

183   where it is subsequently degraded during PINK1/Parkin-dependent mitophagy.

184

185   **Ajuba interacts with PINK1 to promote PINK1 autophosphorylation and mitophagy.**

186   To determine if Ajuba is required for mitophagy, Ajuba $^{-/-}$ MEFs were labeled simultaneously

187   with Mitotracker red and Mitotracker green, treated with CCCP, and the quenching of green

188   fluorescence following acidification in lysosomes was measured by flow cytometry (Sprung et

189   al., 2018). Mitochondrial mass was not different in resting MEFs as measured by Mitotracker

190   green mean fluorescence intensity (MFI) (Figure 3A). However, as indicated by the shift in ratio

191   of red:green MFI following CCCP treatment, mitophagy was reduced in Ajuba$^{-/-}$ MEFs, and not

192   different from WT MEFs treated with CCCP and BafA1 to inhibit lysosomal acidification (Figure

193   3B). This finding suggests that depolarized mitochondria are not delivered efficiently to

194   lysosomes in the absence of Ajuba.

195

196   To determine a functional role for Ajuba in PINK1-Parkin signaling, we turned to the

197   characterized cellular role of Ajuba in relief of kinase autoinhibition, particularly mitotic kinases

198   such as Aurora-A (Kashatus et al., 2011). Similar to these mitotic kinases, human PINK1 is a

199   Ser/Thr kinase whose resting state is in an autoinhibited conformation. However, the

200   mechanism(s) by which this autoinhibition is relieved following stabilization on the outer

201   mitochondrial membrane is not completely characterized (Harper et al., 2018). We

202   hypothesized that once at the mitochondria, Ajuba may bind to PINK1 and function in its

203   recognized role of kinase activation. Ajuba and PINK1 expressed from *E. coli* interacted directly

7

204   with each other by reciprocal co-IP (Figure 3C), a finding that was supported by co-localization

205   of the two proteins in cells by immunofluorescence assay (IFA) (Supplemental Figure 3A).

206   Importantly, *E.coli*-expressed PINK1 has low autophosphorylation activity (Rasool et al., 2018),

207   but auto-phosphorylation of PINK1 at Thr257 significantly increased when PINK1 was incubated

208   with increasing levels of Ajuba (Figure 3D,E). Ajuba can be phosphorylated by the kinase with

209   which it interacts (Chen et al., 2016) prompting us to test if PINK1 phosphorylates Ajuba

210   following coexpression by IP and mass-spectrometry. Based on the PINK1 phosphorylation

211   consensus sequence (Torii et al., 2020), two residues in the pre-LIM domain of Ajuba are

212   predicted to be phosphorylated by PINK1, S39 and S136. Coexpression of PINK1 with Ajuba

213   resulted in a higher molecular mass form of Ajuba (Band 'B'; Supplemental Figure 3B). Peptides

214   visible by mass spectrometry spanned an average of 48% of Ajuba (range 29-63%) and included

215   both of these residues, but only S39 was specifically phosphorylated in the presence of PINK1

216   and not TBK1, another Ser/Thr kinase used as a control (Supplemental Figure 3B). These results

217   demonstrate direct and functional interactions between Ajuba and PINK1.

218

219   To determine if Ajuba affects PINK1 function in cells, we developed an IFA to quantify pSer65-

220   Ub in individual cells. HeLa cells were transfected with HA-Ub, treated with CCCP and stained

221   for pSer65-Ub. The number of puncta were then counted per cell. The assay was validated in

222   HeLa cells lacking either PINK1 or Parkin, demonstrating that pSer65-Ub puncta were

223   dependent on both proteins and coupled to mitochondrial depolarization (Figure 3F,G). Ajuba

224   expression did not induce spontaneous pSer65-Ub puncta, but did increase pSer65-Ub

225   accumulation in CCCP-treated cells compared to a GFP control (Figure 3H). In addition, ectopic

226   expression of Ajuba increased the total level of pSer65-Ub in CCCP-treated cells (Figure 3I).

227   Taken together, these results suggest that Ajuba is required for efficient mitophagy and

228   functions by directly interacting with PINK1 to promote pSer65-Ub accumulation.

229

230   **Zika virus NS5 binds to Ajuba to suppress mitophagy.**

231   To examine the role of Ajuba in mitophagy further, we first determined the effect of ZIKV

232   replication on mitophagy. CCCP-induced pSer65-Ub puncta were markedly reduced in ZIKV-

233   infected cells, suggesting that ZIKV exerts a strong block to mitophagy (Figure 4A). To

234   determine if this was associated with NS5 binding to Ajuba, we first confirmed the interaction.

235   IP of Ajuba resulted in coprecipitation of ZIKV NS5 in HEK293T cells (Figure 4B). ZIKV NS5

236   localizes mainly to the nucleus, but low levels of cytosolic NS5 could be observed co-localizing

237   with Ajuba following co-expression (Figure 4C). Consistent with viral inhibition of mitophagy,

238   ZIKV NS5 reduced accumulation of Ajuba as well as Parkin (used as a downstream target of

239   PINK1) in the mitochondrial fraction following treatment of cells with CCCP (Figure 4D). We

240   also examined localization of Ajuba by IFA with and without NS5 when using MAVS as a

241   stimulus for mitochondrial depolarization. When expressed alone, MAVS localized to

242   mitochondria and caused mitochondrial aggregation (Figure 4E). When Ajuba and MAVS were

243   coexpressed in the same cell, Ajuba appeared to interweave with the mitochondrial marker

244   TOM20 and disrupt aggregates of MAVS (Figure 4F). However, coexpression of ZIKV NS5

245   suppressed mitochondrial recruitment of Ajuba in MAVS-positive cells (Figure 4G). These

246   results suggest that ZIKV imparts a remarkable block to mitophagy that is mediated by NS5

247   binding to Ajuba to suppress its recruitment to depolarized mitochondria.

248

249   **Suppression of mitophagy results in mtRNA release, PKR phosphorylation and PKR-**

250   **dependent chemokine expression.** Perhaps one of the most significant consequences of viral

251   antagonism of mitophagy and failure to clear damaged mitochondria from infected cells is the

252   potential to amplify inflammatory responses (Moehlman and Youle, 2020). To determine the

253   consequence of the viral block in mitophagy, we first performed RNAseq in ZIKV-infected WT,

254   Ajuba$^{-/-}$ or PINK1$^{-/-}$ MEFs. In both mock- and ZIKV-infected cells, the majority of differentially

255   regulated genes (DEGs) were commonly observed in PINK1$^{-/-}$ and Ajuba$^{-/-}$ cells, providing

256   additional evidence that the two proteins function in the same pathway (Figure 5A,B). Notably,

257   ZIKV-infected PINK1$^{-/-}$ and Ajuba MEFs$^{-/-}$ demonstrated increased activation of antiviral and

258   inflammatory pathways (Supplementary Figure 4A). Specifically, chemokines recognized as

259   hallmarks of human infection with ZIKV (Foo et al., 2018; Kam et al., 2017; Michlmayr et al.,

260   2020) were increased by 72 hpi in the absence of Ajuba or PINK1 (Figure 5C and Supplemental

261   Figure 4B). Increased chemokine expression appeared independent of substantial increases in

9

262   virus replication even when IFN signaling was blocked, as measured by release of infectious

263   virus (Figure 5D,E).

264

265   The lack of major differences in viral replication suggests that increased chemokine responses

266   may result from mitochondrial DAMPs. Compared to WT MEFs, mitochondria in ZIKV-infected

267   Ajuba$^{-/-}$ MEFs contained disorganized cristae and loss of double membrane structure suggesting

268   considerable damage (Figure 5F). We also noted from the RNAseq data upregulation of the

269   pathway 'Role of PKR in IFN induction and antiviral response' in ZIKV-infected Ajuba- and

270   PINK1-knockout MEFs (Supplementary Figure 4B, C). PKR is a stress-associated kinase that binds

271   to double stranded RNA (dsRNA) of viral or mitochondrial origin (Kim et al., 2018), or it can be

272   separately activated as part of the integrated stress response (ISR) (Hou et al., 2017). Activated

273   PKR then phosphorylates eIF2α to induce expression of the stress associated transcription

274   factor, ATF4 (Pakos-Zebrucka et al., 2016). In support of the RNAseq data, PKR phosphorylation

275   and ATF4 expression were elevated basally in uninfected Ajuba$^{-/-}$ and PINK1$^{-/-}$ MEFs, and further

276   increased by ZIKV infection (Figure 5 G,H). Mitochondrial RNA (mtRNA) can be visualized using

277   the J2 mAb with high specificity (95-99%) in cultured cells (Dhir et al., 2018). Compared to WT

278   MEFs, mtRNA staining was both increased in intensity and localized outside of mitochondria in

279   the absence of either Ajuba or PINK1 even without additional stimulus for depolarization by

280   CCCP treatment (Figure 5I). To determine if PKR is activated by mtRNA, cells were treated with

281   ethidium bromide (EthBr) to deplete mitochondrial RNA as evidenced by reduced expression of

282   the mitochondrially encoded cytochrome B, but not the nuclear encoded Mfn1. Depletion of

283   mtRNA also suppressed PKR phosphorylation without affecting total PKR expression in ZIKV-

284   infected MEFs (Figure 5 J,K). Taken together, these results provide evidence for release of

285   mtRNA to the cytosol when mitophagy is compromised in primary cells resulting in PKR

286   activation.

287

288   To understand how ZIKV replication, PKR activation, and cytokine expression are linked, we

289   infected primary human dermal fibroblasts with ZIKV and treated the cells with inhibitors of

290   PKR (C16) or eIF2α (ISRIB) phosphorylation (Gal-Ben-Ari et al., 2018; Rabouw et al., 2019). Both

291   inhibitors reduced virus replication consistent with the established roles of PKR in

292   phosphorylating eIF2α (Gal-Ben-Ari et al., 2018) and the known pro-viral role of stress

293   responses that drive eIF2α phosphorylation (Ambrose and Mackenzie, 2011, 2013; Hou et al.,

294   2017)(Figure 6A-C). However, we were surprised to observe that expression of multiple

295   chemokines including CXCL10, CXCL1, CXCL12, CCL2, CCL4, and CCL5, as well as select cytokines

296   (IL-1α and IL-18) were highly dependent on PKR but not eIF2α (Figure 6D-E). Indeed, inhibition

297   of eIF2α-phosphorylation exacerbated chemokine and cytokine expression, consistent with

298   failure to resolve cellular stress through the ISR. Importantly, as virus replication was reduced in

299   both C16- and ISRIB-treated cells, these findings uncouple virus replication from the

300   inflammatory response and support the finding that mtRNA/DAMP signaling is a significant

301   driver of PKR-dependent inflammation. Our data suggests that ZIKV suppression of mitophagy

302   amplifies the ISR which is favorable for flavivirus replication. However, PKR activation in

303   response to mitochondrial damage serves to amplify the pro-inflammatory chemokine response

304   that is the hallmark of flavivirus infection.

305

306   **Pro-inflammatory chemokines are expressed earlier in ZIKV-infected Ajuba$^{-/-}$ mice associated**

307   **with increased virus dissemination to tissues.** To determine the consequences of suppressed

308   mitophagy in vivo, we examined the kinetics of induction of pro-inflammatory cytokines in

309   Ajuba-deficient mice. Using RNAscope assays, *Ajuba* mRNA expression was particularly enriched

310   in epithelial cells of the skin (keratinocytes) and testes (Sertoli cells), and in epithelial and

311   endothelial cells of the lung. *Ajuba* was also expressed in hepatocytes and endothelial cells of

312   the liver, and ependymal cells, neurons, and epithelial cells in the CNS (Supplementary Figure

313   5). Thus, *Ajuba* is expressed in flavivirus target cells and organs. To determine if effects on

314   inflammation can be observed in vivo, WT and Ajuba$^{-/-}$ mice were treated with anti-IFNAR

315   (MAR1) mAb one day prior to footpad inoculation with ZIKV to examine responses in the

316   absence of IFN as a confounding factor in mouse models of ZIKV infection (Gorman et al., 2018;

317   Grant et al., 2016). Viremia was equivalent at 3 and 5 dpi (Figure 7B). However, acute response

318   chemokines were either significantly elevated (CXCL1, CXCL10, CCL7) or trending higher (CCL5,

319   CXCL2) in serum at 3dpi (Figure 7A). In contrast, production of late response cytokines like IFNγ

320   were not affected (Figure 7A). We next examined virus burden in tissues. This revealed the

321   striking finding that virus titers in target tissues including the spleen and brain were up to 80-

322   fold higher at 3dpi in Ajuba$^{-/-}$ mice, despite no differences in viremia. However, by 5 dpi, ZIKV

323   titers in tissues were generally not different between WT and Ajuba$^{-/-}$ mice, demonstrating that

324   there is no intrinsic advantage to virus replication (Figure 7B). These results suggest that

325   suppression of mitophagy by ZIKV facilitates virus invasion of tissue. The pre-treatment of mice

326   with anti-IFNAR mAb suggests that the difference in cytokine expression and virus

327   dissemination at 3 dpi is largely independent of type I or III IFNs, and the equivalent viremia

328   suggests that elevated chemokine expression in serum is not driven by increased viral pattern-

329   associated molecular patterns (PAMPs). Instead, these findings suggest that inhibition of Ajuba

330   and suppressed mitophagy by ZIKV amplifies early expression of acute response chemokines in

331   vivo and that this inflammation is strongly linked to DAMP signaling and virus invasion of

332   tissues.

333

334

335   **DISCUSSION**

336

337   By studying virus-host interactions, this work identifies Ajuba as a critical regulator of PINK1-

338   Parkin-dependent mitophagy. Ajuba participated in mitophagy following multiple stressors,

339   including ER-stress, MAVS activation, or direct mitochondrial depolarization, suggesting that

340   Ajuba is generally important to mitochondrial quality control. ZIKV suppressed PINK1-Parkin-

341   dependent mitophagy early in the pathway prior to the accumulation of pSer65-Ub, consistent

342   with a role for Ajuba in positive regulation of PINK1 activation. PINK1 activation following

343   accumulation on mitochondrial membranes results from self-phosphorylation of the activation

344   loop *in trans* presumably as the local concentration of PINK1 increases (Sekine and Youle,

345   2018). However, we provide several lines of evidence that Ajuba may function to further

346   augment PINK1 activation including demonstration of a direct interaction between PINK1 and

347   Ajuba, augmentation of both PINK1 autophosphorylation in vitro and pSer65-Ub in cells by

348   Ajuba, and RNAseq data suggesting that PINK1 and Ajuba function in overlapping regulatory

12

349   cascades. While the most widely conserved regulatory mechanism for Ser/Thr kinase activation

350   is phosphorylation of kinase activation loop residues, stabilization of conformational changes

351   occurs following kinase binding to cofactors that independently increase kinase activity by up to

352   several hundred-fold (Dodson and Bayliss, 2012; Zorba et al., 2014). Additional careful

353   biochemical studies are needed to determine the precise relationship between PINK1 and

354   Ajuba. However, the identified interaction suggests a potential mechanism for further

355   stabilization of PINK1 conformation to ensure a regulated acceleration of kinase activity, as

356   observed for Aurora-A (Ruff et al., 2018). Further definition of Ajuba's role in PINK1-Parkin

357   signaling may reveal new avenues for therapeutic interventions in PD.

358

359   The consequences of damaged mitochondria to inflammation is currently of intense scientific

360   interest due to the central role of these processes in neurological disorders (e.g. PD, and AD)

361   and cellular transformation. The mechanisms of inflammation are linked to the ancient origins

362   of mitochondria as α-proteobacterium, and are mediated through DAMP activation of innate

363   immune signaling pathways (Mottis et al., 2019; Youle, 2019). For example, mitochondrial DNA

364   is sensed through cGAS-STING, a process that is amplified in PINK1$^{-/-}$ or PARK2$^{-/-}$ deficient mice

365   following metabolic stress (Sliter et al., 2018). mtRNA is also released and can be sensed by PKR

366   or Mda5 (Dhir et al., 2018; Kim et al., 2018). PKR activation by mtRNA and downstream eIF2α

367   phosphorylation has been shown, but role for PKR sensing of mitochondrial health as a central

368   amplifier of chemokine expression during virus infection has not been previously reported.

369   Here, by investigating interactions between ZIKV and mitochondria, we reveal that viral

370   antagonism of mitophagy is directly translated to inflammation through PKR-sensing of mtRNA.

371   Moreover, we show that viral antagonism of mitophagy is a key determinant of virus invasion of

372   tissues linked to pro-inflammatory chemokine responses.

373

374   Pro-inflammatory chemokine expression is linked to disease severity in humans infected with

375   ZIKV, DENV and YFV (Foo et al., 2018; Kam et al., 2017; Michlmayr et al., 2017; Michlmayr et al.,

376   2020; Naveca et al., 2018) although the molecular mechanisms leading to their initial

377   expression are not well defined. As chemokines are ultimately responsible for coordinating

13

378   leucocyte recruitment and activation, determining the early events that drive chemokine

379   expression is a key question in flavivirus pathogenesis. Here we reveal that pro-inflammatory

380   chemokine responses are amplified in ZIKV-infected cells through PKR sensing of damaged

381   mitochondria that are actively retained in cells through viral inhibition of mitophagy. CXCL10

382   and CCL2 have been specifically linked to symptomatic ZIKV infection during pregnancy and

383   congenital abnormalities (Foo et al., 2018; Kam et al., 2017; Naveca et al., 2018). In addition,

384   CXCL10, CCL2, CCL5 and IL-10 have been identified as the central cytokines connecting temporal

385   changes in cell populations and gene expression in the context of ZIKV-infected Nicaraguan

386   children (Michlmayr et al., 2017; Michlmayr et al., 2020). Strikingly, compared to WT mice,

387   Ajuba$^{-/-}$ mice exhibited an earlier amplification of these same cytokines including CXCL10, CCL2,

388   CCL5, and CXCL1 that were similarly elevated at early-acute times in the Nicaraguan cohort,

389   with CCL2, and CXCL10 remaining high during late-acute phase of infection in humans and in

390   our mouse model. Severe disease following flavivirus infection generally occurs after peak virus

391   burden in blood (Tricou et al., 2011). The reasons for this are multifaceted, but our results

392   suggest a specific mechanism for sustained inflammation in tissues due to compromised

393   mitophagy and increased DAMP signaling. As illustrated by infection of primary human

394   fibroblasts, once this signaling is initiated, even a reduction in virus titer through inhibition of

395   the ISR was not sufficient to suppress chemokine expression. Evidence for these processes in

396   humans has been observed in placental tissues from ZIKV-infected mothers including

397   mitochondrial dysfunction, metabolic alterations and induction of inflammatory mediators

398   (Chen et al., 2020). The current work identifies a molecular mechanism for these observations

399   encoded through ZIKV NS5 to amplify mitochondrial stress responses in infected tissue

400   (Supplementary Figure 6). Thus, pathways of mitophagy and DAMP signaling are identified as

401   potential therapeutic targets in severe flavivirus disease.

402

403   Multiple viruses increase mitophagy as a strategy to evade the IFN response (Zhang et al.,

404   2018). Thus, the finding that ZIKV inhibits mitophagy to maintain damaged mitochondria in cells

405   and amplify inflammatory signaling cascades is surprising. The observation that ZIKV encodes at

406   least two mechanisms to manipulate mitochondrial dynamics though NS5 (this paper) and NS4B

14

407   suppression of mitochondrial fission (Chatel-Chaix et al., 2016) suggests that mitochondrial

408   functions are important to virus biology. The pro-viral function of impaired mitophagy will be

409   associated in part with amplification of the ISR as a known factor that favors flavivirus

410   replication through suppression of host mRNA translation (McEwen et al., 2005). However, we

411   observed no fundamental advantage to virus replication in primary MEFs or in mouse tissues

412   lacking Ajuba. Instead, we found that the major consequence of suppressed mitophagy in vivo

413   is to facilitate virus invasion of tissues. The precise events required for flavivirus invasion of

414   critical tissues are not understood (Ayala-Nunez and Gaudin, 2020), although experimental

415   evidence suggests that inflammatory responses could increase virus transmigration across

416   endothelial barriers (Miner and Diamond, 2016). We observed an 80- and 16-fold increase in

417   virus burden in the spleen and brain, respectively, at 3 dpi in Ajuba$^{-/-}$ mice. This increase was

418   independent of viremia levels, intrinsic differences in virus replication, or IFNAR1 signaling, but

419   was associated with earlier expression of chemokines that are considered hallmarks of

420   monocyte recruitment and activation. Monocytes are primary targets for flavivirus infection in

421   the blood (Michlmayr et al., 2017), and ZIKV has been shown to increase monocyte adhesion

422   and transmigration across endothelial barriers (Ayala-Nunez et al., 2019). We therefore

423   speculate that monocyte activation increases tissue seeding of virus. Once in tissues, it is

424   possible that retention of damaged mitochondria in infected cells further promotes tissue

425   injury. To further address these fundamental questions in flavivirus pathogenesis, it will be

426   important to determine the spatial and temporal kinetics of chemokine expression, ZIKV

427   infection and monocyte activation status in blood and key tissues.

428

429   In summary, we have shown that ZIKV NS5 antagonizes mitophagy by binding to the host

430   protein Ajuba and thereby prevents Ajuba translocation to depolarized mitochondria where it is

431   required for PINK1-Parkin signaling. The consequences of this to ZIKV include increased DAMP

432   signaling and increased viral dissemination to tissues. It is well established that viral PAMPs

433   initiate pro-inflammatory responses (Gilfoy and Mason, 2007; Samuel et al., 2006). However,

434   our results suggest that mitochondrial stress leading to release of DAMPs is responsible for

435   amplification of specific chemokines following flavivirus infection, and that this is tightly

436 associated with viral invasion of tissues. Suppression of mitophagy also provides a potential

437 selection pressure for development of flavivirus strategies to antagonize IFN responses

438 downstream of mitochondria including suppression of cGAS-STING signaling to mitigate mtDNA

439 release (Aguirre et al., 2017; Aguirre et al., 2012; Yu et al., 2012), and the property of NS5 as a

440 very potent JAK-STAT antagonist to suppress downstream IFN signaling in infected cells (Best,

441 2017). In addition, ZIKV encodes blocks to RLR-MAVS signaling downstream of MAVS, including

442 suppression of TBK1 and IRF3 activation (Xia et al., 2018). Moreover, these findings raise new

443 potential mechanisms of immune activation and dysfunction in the context of flavivirus

444 infection based on recognized roles of mitophagy in suppressing DAMP-driven responses and

445 autoimmunity (reviewed in (Mottis et al., 2019; Youle, 2019). Finally, our findings illustrate a

446 role of mitophagy in protection from inflammatory responses and virus infection in vivo,

447 beyond the context of neurodegeneration. It is noteworthy that therapeutics aimed at

448 augmentation of mitophagy improve cellular function in animal models of AD (Fang et al.,

449 2019). Thus, therapeutics under development for PD, AD and other disorders of mitochondrial

450 dysfunction should be considered for testing in flavivirus infection models. In this case,

451 augmented mitophagy may dampen pro-inflammatory responses and limit virus seeding of

452 tissues.

453

454

455 **Acknowledgements**

462

463 **Author contributions**

464   Conceptualization, S.S.P. and S.M.B; Methodology, S.S.P., S.J.R., K.L.M., F.J., C.S., C.M. and

465   S.M.B.; Investigation, S.S.P., S.J.R., K.L.M., G.L.S., M.L., F.J., C.K., D.G., A.H., C.S., R.R., G.S., and

466   C.M.; Resources, C.M.B, G.S., C.M., and S.M.B.; Data curation, S.S.P., S.J.R., K.L.M., G.L.S., M.L.,

467   F.J., C.K., C.S., G.S., C.M., and S.M.B.; Writing – original draft, S.S.P. and S.M.B; Writing – Review

468   and Editing, S.S.P., S.J.R., K.L.M., G.L.S., M.L., F.J., and S.M.B.; Visualization, S.S.P. and S.M.B;

469   Supervision, S.J.R., C.M.B., G.S., C.M. and S.M.B.

470

471   **Declaration of Interests**

472   The authors declare no competing interests.

473

474

475

476

477

478   **METHODS**

479

480   **Cell Culture and generation of Mouse embryonic fibroblasts (MEFs)**

481   HEK293T cells (ATCC; CRL-3216), HEK293 cells (ATCC; CRL-1573), A549 cells (ATCC; CCL-185),

482   Human hepatoma cell line (Huh7), Vero cells (ATCC; CCL-81), Hela cells (ATCC; CCL-2) and

483   PINK1/Parkin modified Hela cells (Ordureau et al., 2014), Primary Dermal Fibroblast (ATCC; PCS-

484   201-012) and murine embryonic fibroblasts (WT MEF), Ajuba$^{-/-}$ and PINK1$^{-/-}$ MEFs were grown in

485   Dulbecco's modified enrichment medium (GIBCO; 11995-065) containing 10% fetal bovine serum

486   (GIBCO; 16000-044) and 1% penicillin/streptomycin (GIBCO; 15140-122) in an atmosphere of 5%

487    $CO2$ at 37°C. For WT, PINK1$^{-/-}$ and Ajuba$^{-/-}$ MEFs isolation, fifteen-day old mouse embryos were

488   collected, their separated torsos were washed with PBS, minced, placed in 0.25 % trypsin-EDTA

489   (Invitrogen) containing 1 µg/ml DNase I (Ambion) and incubated at 37°C for 15 min. Cells were

490   filtered using a 100 µM nylon strainer, centrifuged (500 x g, 5 min), resuspended in complete

491   DMEM, plated in tissue culture flasks with designation of passage 1. These cells were used for

492   experiments between passage 2-5. All cells were counted on an Image Cytometer (Invitrogen).

493   Cells were either mock infected or infected with SENV (200 Units/well; Charles River

494   Laboratories), VSV (MOI 0.01) and ZIKV PRABC59 strain (MOI 1). Virus was allowed to adsorb for

495   1 hour at 37°C followed by a media change and incubation for the indicated time.

496

497   **Plasmids, siRNAs and Transfections**

498   Human Ajuba and LIMD1 genes were PCR amplified from cDNA templates and directionally

499   cloned into the Gateway entry vector pENTR/SD/D-TOPO (ThermoFisher). Mammalian

500   expression plasmids were then obtained by recombination into Gateway destination vectors

501   pcDNA6.2/FLAG-DEST, GFP-DEST and RFP-DEST (for N-terminal FLAG tag, N'-GFP tag and N'-RFP
502   tag). All plasmids were verified by DNA sequencing. Additional plasmids used to express GFP,
503   MAVS and HA-Ubiquitin were obtained from Addgene (#135046, #52135 and #17608) while
504   EGFP-Parkin and its mutant was a kind gift from Dr. Wolfdieter Springer (Mayo Clinic, Jacksonville
505   FL). ZIKV virus NS5 expression plasmids are previously described (Grant et al., 2016). For siRNA
506   experiments, A549 cells in a 12-well format were transfected with 10 pmol of siRNA (Dharmacon;
507   SMART pool against AJUBA, LIMD1 mRNA and a nonspecific control sequence) for 48 h using
508   Lipofectamine RNAiMAX (Life Technologies). Plasmid transfections were performed according to
509   manufacturer's protocol in 12 -well plates or 4-well Lab Tek II chamber slides (Nunc) using
510   jetPRIME reagent (VWR INTERNATIONAL; # 89129-924). For harder to transfect Huh7 cells a
511   spinning method was performed post transfection (Spinfection) that adds centrifugation of
512   transfected cells at 1000 rpm for 30 minutes at rt.

513

514   **Western Blotting**
515   Cells were washed in phosphate buffered saline (PBS) and harvested in 300 μl each (for 12 well
516   plate) and 500 μl each (for 6 well plate) in RIPA buffer (50 mM Tris-HCl, 150 mM NaCl, 0.1 % SDS,
517   1% NP-40, 0.5% Na-deoxycholate and DNase I) with complete protease and phosphatase
518   inhibitor cocktail (Roche). Cellular debris was removed by centrifugation (10000 x g for 10 min at
519   4°C) and the supernatant was mixed with sample buffer (2X SB, 62.5 mM TRIS pH 6.8, 10%
520   glycerol, 15 mM EDTA, 4% 2-ME, 2% SDS, and bromophenol blue) and incubated for 10 min at
521   95°C. An equal amount of sample was resolved by electrophoresis in the presence of SDS on
522   polyacrylamide gels (ThermoFisher). Proteins were transferred to nitrocellulose/PVDF
523   membrane using the iBlot Gel Transfer Device (ThermoFisher) or wet transferred using 0.5 M
524   sodium phosphate transfer buffer (at a constant 1 Amp for an hour using a Bio-Rad apparatus).
525   Membranes were blocked in 5% milk in PBS-T and probed with primary antibody (overnight at
526   4˚C) followed by an hour incubation with secondary antibody at rt with 3X washes of PBST for 10
527   minutes after each step of incubation. Membranes were blocked in membrane blocking solution
528   (ThermoFisher) with 50mM NaF added when phospho-specific antibodies were used.
529   Immunoreactive proteins were detected by the ECL Plus chemiluminescent system (Thermo
530   Fisher). Western blots were scanned using FluorChem E system (Protein Simple) and
531   quantification of immunoblot bands was performed using ImageJ software.

532

533   **Antibodies**
534   The following primary antibodies were used: mouse anti FLAG (#F1804-200UG, Sigma), rabbit
535   anti FLAG tag (#8146S and #14793S, Cell Signaling Technology), mouse anti HA tag (#901502,
536   Biolegend), rabbit anti HA tag (#3724S, Cell Signaling Technology), mouse anti GFP (#632381,
537   Takara Bio Clontech), mouse anti Vinculin (#V9131-100UL, MilliporeSigma), mouse anti GAPDH
538   (#sc-47724, Santa Cruz), mouse anti Ajuba (#sc-374610, Santa Cruz), rabbit anti Ajuba (#34648S
539   and #4897S, Cell Signaling Technology), rabbit anti p-Ubiquitin Ser65 (#ABS1513-I, EMD
540   Millipore), rabbit anti p-Ubiquitin Ser65 (#37642S, Cell Signaling Technology), mouse anti
541   Mitofusin-2 (#sc-100560, Santa Cruz), rabbit anti Mitofusin-1 (#sc-50330, Santa Cruz), rabbit anti
542   Mitofusin-1 (#14739S, Cell Signaling Technology), mouse anti MAVS (#ENZ-ABS259-0100, Enzo),
543   rabbit anti TIM44 (#ab24466, Abcam), rabbit anti-TOMM20 (#HPA011562, Sigma), rabbit anti
544   Calreticulin (#JM-3077-100, MBL international Corporation), rabbit anti PINK1 (#ab23707,

545 Abcam), mouse anti PINK1 (#sc-517353, Santa Cruz), sheep anti p-PINK1 Thr-257 (#68-0057-100,
546 Ubiquigent), mouse anti Parkin (#sc-32282, Santa Cruz), rabbit anti Parkin (#2132S, Cell Signaling
547 Technology), rabbit anti PKR (#ab184257, Abcam), rabbit anti p-PKR Thr-451 (#07-886, EMD-
548 Millipore), rabbit anti eIF2a (#9722S, Cell Signaling Technology), rabbit anti p-eIF2a S51 (#9721S,
549 Cell Signaling Technology), rabbit anti ATF4 (#11815S, Cell Signaling Technology), dsRNA antibody
550 J2 (#10010200, English& Scientific Consulting), mouse anti ZIKV Envelope (#BF-1176-56, BioFront
551 Technologies) and chicken antibody to SENV (#ab33988, Abcam). Mouse isotype IgG control (#sc-
552 2025, Santa Cruz) and rabbit isotype IgG control (#sc-2027, Santa Cruz) was used as a control for
553 immunoprecipitation. Following secondary antibodies were used: HRP conjugated goat anti-
554 mouse antibody (#P0447, Dako from Agilent), HRP conjugated goat anti-rabbit antibody (#P0448,
555 Dako from Agilent), anti-chicken antibodies (#12-341, Millipore) and anti-sheep HRP Secondary
556 antibody (#ab97125, Abcam).
557
558 **Inhibitors**
559 Cell culture grade proteasomal inhibitors epoxomicin (Sigma; #E3652) and lysosomal inhibitor
560 bafilomycin A1 (Baf-A1) (Sigma; #B1793) was used at concentration of 200nM each. Oxidative
561 stress inducers tunicamycin (Sigma; # SML1287) and oligomycin A (Sigma; # 75351) were used at
562 5μg/ml for 5 h in incomplete media. Mitochondrial depolarizing agent carbonyl cyanide 3-
563 chlorophenylhydrazone, CCCP (Millipore Sigma; #C2759) was used at 10μM. Integrated stress
564 response inhibitors ISRIB (Sigma; #SML0843), PKR inhibitor C16 (Millipore Sigma; #527450) and
565 a PKR Inhibitor negative control (Millipore Sigma; #527455) were used at 500nM for 24 h prior to
566 the time of harvest. Ethidium bromide solution (Sigma; #E1385) was used at 100ng/ml.
567
568 **Generation of Knockout Mice**
569 Ajuba knockout mice ($Ajuba^{-/-}$) were generated using CRISPR/Cas9 technology. Briefly, in vitro
570 synthesized guide RNA (sgRNAs) that were designed to cut shortly after the translation initiation
571 codon in Ajuba Exon 1 were ordered from ThermoFisher's sgRNA service
572 (CCGGAGTCCGAGAGTCTCAACTT). sgRNA (20ng/ul) was microinjected with Cas9 mRNA (50ng/ug
573 purchased from TriLink BioTechnologies) into the cytoplasm of fertilized eggs collected from
574 C57BL/6N mice (Charles River Laboratory). The injected embryos were cultured overnight in M16
575 medium, and those that reached 2-cell stage of development were implanted into the oviducts
576 of pseudopregnant foster mothers (CD-1 mice from Charles River Laboratory). Offspring born to
577 the foster mothers were genotyped by PCR and sanger sequencing. Founder mice with desired
578 mutations were bred with C57BL/6NJ mice to establish the knockout mouse line. The two lines
579 #1 (with 4 nt deletion) and #2 (with 22 nt deletion in exon 1) were designated as Ajuba$^{-/-}$ 8216A
580 and Ajuba$^{-/-}$ 8258B respectively. The PINK1 knockout mice (PINK1$^{-/-}$) were procured from Jackson
581 Laboratory.
582
583 **Mouse experiments**
584 All animal experiments were approved by the IACUC of Rocky Mountain Laboratories, National
585 Institutes of Health and carried out by a certified staff in an Association for Assessment and
586 Accreditation of Laboratory Animal Care International accredited facility, according to the
587 institution's guidelines for animal use, and followed the guidelines and basic principles in the U.S.
588 Public Health Service Policy on Humane Care and Use of Laboratory Animals and the Guide for

589 the Care and Use of Laboratory Animals. Male and female mice (4-5 weeks old) were treated by
590 intraperitoneal injection with 2 mg of an anti-mouse IFNAR1 blocking antibody (MAR1-5A3, from
591 Leinco Technologies). The next day, mice were inoculated subcutaneously (via footpad) with 10^3
592 PFU of mouse-adapted ZIKV-Dak-41525 (Gorman et al., 2018) kindly provided by Dr. Michael
593 Diamond (University of Washington School of Medicine in Saint Louis). Tissue and blood samples
594 were collected on day 3 and 5 post infection.
595
596 **RNA Isolation and quantitative RT-PCR**
597 Total RNA was isolated from cells using RNeasy kit with genomic DNA elimination (QIAGEN). RNA
598 was reverse transcribed using a SuperScript VILO cDNA synthesis kit (ThermoFisher) according to
599 manufacturer's protocol. cDNA was then used as a template in TaqMan-PCR reactions per
600 manufacturer's instructions (Applied Biosystems) to quantify mRNA specific for IFNβ (assay ID:
601 Hs01077958_s1), housekeeping gene HPRT (assay ID: Hs01003267_m1), Ajuba (assay ID:
602 Hs00262750_m1) and LIMD1 (assay ID: Hs01040528_m1). Reactions for Real-time RT-PCR were
603 set up in triplicate, cycled and data was collected on the Applied Biosystems GeneAmp 9500
604 Sequence detection system. Gene expression was normalized to HPRT mRNA levels and
605 expressed as fold change relative to RNA samples from control cells using the comparative ΔCT
606 method.
607
608 **Plaque assay**
609 Viral titers from supernatants collected from cells infected with VSV or ZIKV were determined by
610 plaque assay. Briefly, 24 hr prior to titrations, 24-well plates were seeded with 2×10^5 Vero cells
611 per well. Viral samples were 10-fold serially diluted in completed DMEM ranging from 10^{-1} to 10^{-8}
612 and 125 μl of dilution was added to individual wells. After the plates were incubated for 1h of
613 virus adsorption, the inoculum was removed, and the cells were overlaid with Minimum Essential
614 Medium containing 1.5% carboxymethylcellulose (w/v). The plates were incubated at 37°C for 4
615 days and were then fixed with 10% formaldehyde for 1 hr at rt followed by staining with 1%
616 crystal violet (in 25% ethanol) for 10 min. Excessive crystal violet and residual overlay media was
617 washed with water and visible plaques were counted to calculate viral titers as plaque forming
618 units per ml (PFU/ml). For analysis of viral distribution in tissues, mice were euthanized at 3 and
619 5 dpi, and indicated tissues were collected. Organs were individually weighed, homogenized, and
620 prepared as 10% (w/v) suspensions in DMEM/2% FBS/Pen/Strep. Suspensions were then clarified
621 by centrifugation (4,000 rpm for 5 min at 4°C), and the supernatants were titrated using plaque
622 assay.
623
624 **Confocal Microscopy**
625 80,000 cells were seeded onto each well of 4 well Lab-Tek II chamber slides (Thermo Fisher
626 Scientific) overnight. To fix, cells were washed with PBS and subsequently fixed with 4%
627 paraformaldehyde for 10 min. Cells were permeabilized with 0.1% Triton X-100 for 5 min at RT,
628 and incubated with blocking solution (PBS, 0.5% BSA, 1% goat serum) for an additional 30 min.
629 Cells were then incubated with primary antibody overnight at 4°C (or 2 hours at RT), washed
630 three times with PBS and further incubated with secondary antibody (in blocking buffer)
631 conjugated to Alexa 488, 594 or 647 (Thermo Fisher Scientific) for 1 h. Slides were washed three
632 times with PBS and once with miliQ water, and mounted onto glass coverslips using Prolong Gold

633   Antifade Reagent with DAPI (Invitrogen). Processed slides were imaged using a Zeiss LSM710

634   confocal microscope and further analyzed using Zen software (Carl Zeiss).

635

636   **Mitochondrial Fractionation**

637   Mitochondria Isolation Kit for Cultured Cells (Thermo Fisher Scientific; # 89874) was used for

638   mitochondrial fractionation using the manufacturer's protocol. In short, around 2×10^7 cells were

639   pelleted by centrifugation in a 2.0mL microcentrifuge tube at $850 \times g$ for 2 minutes. Supernatant

640   was discarded and 800 µL of Mitochondria Isolation Reagent A (with proteasomal inhibitor) was

641   added. Cells were vortexed at medium speed for 5 seconds and incubated on ice for exactly 2

642   minutes. 10 µL of Mitochondria Isolation Reagent B was added and sample was vortexed at

643   maximum speed for 5 seconds followed by an incubation on ice for 5 min with an in between

644   vortexing step at maximum speed every minute. 800 µL of Mitochondrial Isolation Reagent C

645   (with proteasomal inhibitor) was added and the sample tube was inverted several time to mix

646   properly. The sample was centrifuged at 700 $\times g$ for 10 minutes at 4°C and the supernatant was

647   transferred to a new 2.0 ml tube, followed by another centrifugation step at 12,000 $\times g$ for 15 min

648   at 4°C. The pellet contains the isolated mitochondria and supernatant is cytosolic fraction.

649   Mitochondrial pellet was given an additional wash using 500 µL of Mitochondria Isolation

650   Reagent C and centrifugation step at 12,000 $\times g$ for 5 minutes. The pellet was dissolved directly

651   in 60 µL of lamelli buffer for western blotting as a downstream application and meanwhile stored

652   in -20°C.

653

654   **Extracellular Flux (Seahorse) Analysis.**

655   MEF isolated from WT, PINK1^{-/-}, or and AJUBA^{-/-} mice were seeded at 2×10^4 cells per well in a

656   XFe96 tissue culture plate and incubated for 24 hours in cDMEM. Cells were washed 2 times with

657   200 µL of extracellular flux assay medium (DMEM with 25 mM glucose, 2 mM sodium pyruvate,

658   and 2 mM L-glutamine for mitochondrial stress test (Agilent Technologies). Assay medium was

659   then added to each well to make the final well volume 180 uL. Cells were incubated for 1 hr at

660   37°C in a non-CO_2 incubator prior to extracellular flux analysis. Oxygen consumption rate (OCR)

661   rate was measured using the Mito Stress Test according to manufactures instructions. Briefly,

662   mitochondrial stress assessment included analysis of basal OCR and OCR following injection of

663   oligomycin (2 µM, MilliporeSigma), fluoro-carbonyl cyanide phenylhydrazone (FCCP; 2 µM;

664   Cayman Chemical), and rotenone/antimycin (0.5 µM final concentration for both;

665   MilliporeSigma). All extracellular flux assays were performed on the Seahorse XFe96 Analyzer

666   (Agilent Technologies).

667

668   **Flow cytometry**

669   Cells were harvested after 16 hours of treatment conditions, and 30 minutes of mitotracker

670   staining (200nM)(Sprung et al., 2018) followed by staining with LIVE/DEAD Fixable Aqua Dead

671   Cell Stain Kit (ThermoFisher). Data was acquired on a LSRII flow cytometer (BD Biosciences) and

672   analyzed using FlowJo software and are representative of four independent experiments

673   performed. Dead cells, debris and doublets were excluded from all analyses.

674

675   **Protein Purification (By GeneScript)**

676 Ajuba and PINK1 DNA sequence was codon optimized and synthesized to be cloned into pET30a
677 vector with N terminal His tag for protein expression in *E. coli*. Transformed *E. coli* strain
678 BL21(DE3) was inoculated into TB medium containing kanamycin and cultured at 37 °C. When
679 the OD600 reached about 1.2, cell culture was induced with IPTG at 15°C for 16 h. Cells were
680 harvested by centrifugation. Cell pellets were resuspended with lysis buffer followed by
681 sonication. The inclusion bodies after centrifugation were dissolved using urea. Target protein
682 from denatured supernatant were refolded and sterilized by 0.22μm filter. Protein concentration
683 was determined by Bradford protein assay with BSA as standard. The protein purity and
684 molecular weight were determined by standard SDS-PAGE along with western blot confirmation.
685

686 **Co-immunoprecipitation assay (co-IP)**
687 Cells were washed with PBS and lysed in RIPA buffer (supplemented with 5μg/ml DNAse I and
688 protease inhibitor cocktail). Samples were subjected to centrifugation for 10 min to remove
689 cellular debris and 100 μL of supernatant was reserved for input analysis. Cell lysates were then
690 pre-cleared by addition of Dynabeads Protein G (ThermoFisher) and rotated at 4°C for 3 h. Beads
691 were removed by centrifugation, and 2 μg antibody (corresponding to the protein of interest/
692 protein tag) was added to each lysate for 2 h with rotation at 4°C. 50 μL of Dynabeads Protein G
693 were added again, and lysates were incubated with rotation at 4°C overnight. Lysates were
694 discarded after a brief centrifugation, and beads were washed 3 times in RIPA buffer for 15 min
695 (at 4°C with rotation) prior to elution by incubation at 95°C for 10 minutes in 50 μL of 2X sample
696 buffer. The eluted samples were assayed by immunoblotting as described above. IP with *E.coli*
697 purified PINK1 and Ajuba used 250nM of each protein in PBS followed by the regular protocol
698 past the preclear step.
699

700 *In-vitro* **PINK1 phosphorylation assay**
701 Kinase assay was performed using recombinant proteins purified from *E.coli* and commercially
702 available 10X Kinase buffer (Cell Signaling Technology, #9802). Recombinant proteins (N'-His
703 PINK1 and N'-His Ajuba) were thawed on ice. In a clean microtube, 500 μM ATP in kinase assay
704 buffer diluted in miliQ water to a final concentration of 1× and PINK1 (300 nM) was mixed with
705 Ajuba, the concentration of which was adjusted by dilution from 50 nM to 300 nM for each
706 separate kinase reaction in 25 μl total reaction volume. All reaction mixtures were normalized
707 with BSA to have 1ug total protein in each condition. Negative controls were prepared using as
708 above with either minus Ajuba or minus PINK1. Reactions were spin down for 10 sec at $1,000 \times g$
709 at 4 °C and then were incubated in heated shaker at 30 °C for 30 minutes. The reaction was
710 stopped by boiling for 5 min at 95 °C in 6× SDS loading buffer and were separated by SDS-PAGE
711 electrophoresis (16% gel). Detection of PINK1 auto phosphorylation was assessed using phospho-
712 specific antibody on a western blot.
713

714 **Bio-plex Cytokine Analysis**
715 Sera were collected from mock- and ZIKV-infected mice at 3 and 5 dpi. Primary human dermal
716 fibroblast culture supernatants were collected at the indicated time points after ZIKV infection
717 and Control/C16/ISRIB treatment. Cytokine concentrations in serum were measured using a
718 mouse 23-cytokine Bio-Plex Pro Assay according to the manufacturer's instructions (BioRad).
719 Concentrations for human cytokines were determined using the ProcartaPlex Multiplex

720 Immunoassay (Thermo Fisher Scientific). Briefly, samples were incubated with magnetic beads
721 coupled to cytokine-specific antibodies for 2 h at rt. Beads were washed, incubated with biotin-
722 labeled secondary antibodies for 30 min, washed again and then incubated with a streptavidin
723 reporter for 30 min. After another round of washing, resuspended beads were read by Luminex
724 200 Bio-Plex Array Reader (Bio-Rad) to acquire data (Internal bead fluorescence, indicative of
725 each distinct cytokine, and fluorescence intensity of signal).
726

Electron Microscopy

728 Cells were grown on Thermanox coverslips and fixed with 2.5% glutaraldehyde in 0.1 M sodium
729 cacodylate buffer. Samples were processed in a PELCO BioWave laboratory microwave (Ted Pella,
730 Reading, California) by post-fixation with 0.5% osmium tetroxide + 0.8% potassium ferrocyanide
731 in 0.1 M sodium cacodylate buffer, buffer rinse, 1% aqueous tannic acid, water rinse, 1% aqueous
732 samarium acetate, water rinse, dehydration into ethanol, embedment into epon, and
733 polymerization overnight at 60°C. Thin sections were cut with a Leica UC6 ultramicrotome (Leica
734 Microsystems, Vienna, Austria), stained with uranyl acetate, and imaged on either a 120 kV
735 HT7800 (Hitachi) operating at 80 kV with an XR-81B CMOS digital camera (AMT Imaging System,
736 Woburn, Massachusettes) or on a 120 kV Tecnai Bio Twin Spirit (FEI, Hillsboro, Oregon) with a
737 Rio CMOS digital camera (Gatan, Pleasanton, California).
738

NGS Library Preparation

740 Cells were harvested in Trizol and frozen on dry ice. Each sample lysate was combined with
741 additional Trizol to bring the final volume to 1000µl in each sample, 200µl of 1-Bromo-3-
742 chloropropane (MilliporeSigma) was added, samples mixed, and centrifuged at 16,000 x g for 15
743 min at 4°C. RNA containing aqueous phase of 600µl was collected from each sample and passed
744 through Qiashredder column (Qiagen) at 21,000 x g for 2 min to homogenize any remaining
745 genomic DNA in the aqueous phase. Aqueous phase was combined with 600µL of RLT lysis buffer
746 (Qiagen) with 1% β mercaptoethanol and RNA was extracted using Qiagen AllPrep DNA/RNA 96-
747 well system. An additional on-column Dnase I treatment was performed during RNA extraction.
748 Standard RNeasy extraction protocol resulted in RNAs larger than 200nt. All sample processing
749 was performed using amplicon-free reagents and tools in aerosol resistant vials. RNA was
750 quantitated by spectrophotometry and RNA yield ranged from 0.6 to 8.5µg. RNA quality was
751 analyzed using Agilent 2100 Bioanalyzer (Agilent Technologies) and RNA integrity number (RIN)
752 ranged from 7.6 to 9.9 (showing an overall exceptional RNA quality). 500 ng RNA was used as
753 input for the TruSeq Stranded mRNA-Seq Sample Preparation Kit (Illumina). The protocol was
754 followed without modification. Final library size distribution was assessed on a BioAnalyzer DNA
755 1000 chip (Agilent Technologies). The average size of the libraries was on target at around 310
756 bp. Libraries were quantified using the Kapa SYBR FAST Universal qPCR kit for Illumina sequencing
757 on the CFX384 Real-Time PCR Detection System (Bio-Rad Laboratories). The libraries were diluted
758 to 4 nM stocks and pooled equitably for sequencing. The 4 nM pool of libraries was prepared for
759 sequencing by denaturing and diluting to a 1.8 pM stock for clustering to the flow cell. On-board
760 cluster generation and paired-end sequencing was completed on the NextSeq 550 (Ilumina) using
761 a High Output 150 cycle kit (Illumina). The average cluster density was 177 k/mm^2 resulting in
762 420 million reads passing filter per run, with an average of 22.6 million reads per sample. Raw
763 fastq reads were trimmed of Illumina adapter sequences using cutadapt version 1.12 and then

23

764 trimmed and filtered for quality using the FASTX-Toolkit (Hannon Lab). Remaining reads were
765 aligned to the mouse genome assembly mm10 using Hisat2. Reads mapping to genes were
766 counted using htseq-count.
767
768 **Bioinformatic analysis**
769 Briefly, differential expression analysis in heatmaps was performed using the Bioconductor
770 package DESeq2. Cytokine analysis for RNA seq data involves 157 genes mapped on the KEGG
771 pathway mmu04060. Volcano plots were created to identify cytokine genes showing more than
772 2 log2 fold change with corresponding significant P values in control versus infected samples.
773 Functional and network analysis of statistically significant gene expression changes was
774 performed using Ingenuity Pathways Analysis (IPA, QIAGEN). Significant canonical pathways are
775 identified from IPA based on enrichment of the zscore.
776
777 **Mass spectrometry (By MS Bioworks)**
778 Samples were processed by SDS-PAGE using a 4-12% Bis-Tris NuPAGE gel (Invitrogen) with the
779 MOPS buffer system. The target bands were excised and processed by in-gel digestion using a
780 robot (ProGest, DigiLab). The digest was analyzed by nano LC-MS/MS with a Waters NanoAcquity
781 HPLC system interfaced to a ThermoFisher Q Exactive. Peptides were loaded on a trapping
782 column and eluted over a 75μm analytical column at 350nL/min; both columns were packed with
783 Luna C18 resin (Phenomenex). The mass spectrometer was operated in data-dependent mode,
784 with the Orbitrap operating at 60,000 FWHM and 17,500 FWHM for MS and MS/MS respectively.
785 The fifteen most abundant ions were selected for MS/MS. Samples were analyzed in analytical
786 duplicate. Data were searched using a local copy of Mascot (Matrix Science) and Mascot DAT files
787 were parsed into Scaffold (Proteome Software) for validation, filtering and to create a non-
788 redundant list per sample. Data were filtered using a minimum protein value of 99.9%, a
789 minimum peptide value of 50% (Prophet scores) and requiring at least two unique peptides per
790 protein. Scaffold results were exported as mzidentML and imported in to Scaffold PTM in order
791 to assign site localization probabilities using A-score with minimum localization probability filter
792 of 50%.
793
794 **RNA scope in-situ Hybridization**
795 In situ hybridization was performed using the RNAScope 2.5 VS assay (Advanced Cell Diagnostics,
796 Newark, CA) according to the manufacturer's instructions using a mouse Ajuba specific probe
797 (cat#579019).
798
799 **Statistical Analysis.**
800 All data were evaluated for significance using student T-tests, Mann Whitney test, or one-
801 way/two-way ANOVA with appropriate multiple comparison post tests using GraphPad Prism 7
802 software. Statistical significance was assigned as when p values were <0.05. Specifically, *p<0.05,
803 **p<0.01, ***p<0.001, ****p<0.0001, not significant (NS) when p > 0.5.
804
805 **References for Methods:**

24

806   Gorman, M.J., Caine, E.A., Zaitsev, K., Begley, M.C., Weger-Lucarelli, J., Uccellini, M.B., Tripathi,
807   S., Morrison, J., Yount, B.L., Dinnon, K.H., 3rd*, et al.* (2018). An Immunocompetent Mouse
808   Model of Zika Virus Infection. Cell Host Microbe *23*, 672-685 e676.
809
810   Grant, A., Ponia, S.S., Tripathi, S., Balasubramaniam, V., Miorin, L., Sourisseau, M., Schwarz,
811   M.C., Sanchez-Seco, M.P., Evans, M.J., Best, S.M.*, et al.* (2016). Zika Virus Targets Human STAT2
812   to Inhibit Type I Interferon Signaling. Cell Host Microbe *19*, 882-890.
813
814   Ordureau, A., Sarraf, S.A., Duda, D.M., Heo, J.M., Jedrychowski, M.P., Sviderskiy, V.O.,
815   Olszewski, J.L., Koerber, J.T., Xie, T., Beausoleil, S.A.*, et al.* (2014). Quantitative proteomics
816   reveal a feedforward mechanism for mitochondrial PARKIN translocation and ubiquitin chain
817   synthesis. Mol Cell *56*, 360-375.
818
819   Sprung, M., Dikic, I., and Novak, I. (2018). Flow Cytometer Monitoring of Bnip3- and Bnip3L/Nix-
820   Dependent Mitophagy. Methods Mol Biol *1759*, 105-110.
821
822
823
824
825

826   **References for Main Text:**

827   Aguirre, S., Luthra, P., Sanchez-Aparicio, M.T., Maestre, A.M., Patel, J., Lamothe, F., Fredericks,
828   A.C., Tripathi, S., Zhu, T., Pintado-Silva, J.*, et al.* (2017). Dengue virus NS2B protein targets cGAS
829   for degradation and prevents mitochondrial DNA sensing during infection. Nat Microbiol *2*,
830   17037.
831
832   Aguirre, S., Maestre, A.M., Pagni, S., Patel, J.R., Savage, T., Gutman, D., Maringer, K., Bernal-
833   Rubio, D., Shabman, R.S., Simon, V.*, et al.* (2012). DENV inhibits type I IFN production in infected
834   cells by cleaving human STING. PLoS Pathog *8*, e1002934.
835
836   Ambrose, R.L., and Mackenzie, J.M. (2011). West Nile virus differentially modulates the
837   unfolded protein response to facilitate replication and immune evasion. J Virol *85*, 2723-2732.
838
839   Ambrose, R.L., and Mackenzie, J.M. (2013). ATF6 signaling is required for efficient West Nile
840   virus replication by promoting cell survival and inhibition of innate immune responses. J Virol
841   *87*, 2206-2214.
842
843   Archer, S.L. (2013). Mitochondrial dynamics--mitochondrial fission and fusion in human
844   diseases. N Engl J Med *369*, 2236-2251.
845

846 Ayala-Nunez, N.V., Follain, G., Delalande, F., Hirschler, A., Partiot, E., Hale, G.L., Bollweg, B.C.,
847 Roels, J., Chazal, M., Bakoa, F*., et al.* (2019). Zika virus enhances monocyte adhesion and
848 transmigration favoring viral dissemination to neural cells. Nat Commun *10*, 4430.

850 Ayala-Nunez, N.V., and Gaudin, R. (2020). A viral journey to the brain: Current considerations
851 and future developments. PLoS Pathog *16*, e1008434.

853 Best, S.M. (2017). The Many Faces of the Flavivirus NS5 Protein in Antagonism of Type I
854 Interferon Signaling. J Virol *91*, e01970-16.

856 Chatel-Chaix, L., Cortese, M., Romero-Brey, I., Bender, S., Neufeldt, C.J., Fischl, W., Scaturro, P.,
857 Schieber, N., Schwab, Y., Fischer, B*., et al.* (2016). Dengue Virus Perturbs Mitochondrial
858 Morphodynamics to Dampen Innate Immune Responses. Cell Host Microbe *20*, 342-356.

860 Chen, Q., Gouilly, J., Ferrat, Y.J., Espino, A., Glaziou, Q., Cartron, G., El Costa, H., Al-Daccak, R.,
861 and Jabrane-Ferrat, N. (2020). Metabolic reprogramming by Zika virus provokes inflammation in
862 human placenta. Nat Commun *11*, 2967.

864 Chen, X., Stauffer, S., Chen, Y., and Dong, J. (2016). Ajuba Phosphorylation by CDK1 Promotes
865 Cell Proliferation and Tumorigenesis. J Biol Chem *291*, 14761-14772.

867 Dhir, A., Dhir, S., Borowski, L.S., Jimenez, L., Teitell, M., Rotig, A., Crow, Y.J., Rice, G.I., Duffy, D.,
868 Tamby, C*., et al.* (2018). Mitochondrial double-stranded RNA triggers antiviral signalling in
869 humans. Nature *560*, 238-242.

871 Dodson, C.A., and Bayliss, R. (2012). Activation of Aurora-A kinase by protein partner binding
872 and phosphorylation are independent and synergistic. J Biol Chem *287*, 1150-1157.

874 Fang, E.F., Hou, Y., Palikaras, K., Adriaanse, B.A., Kerr, J.S., Yang, B., Lautrup, S., Hasan-Olive,
875 M.M., Caponio, D., Dan, X*., et al.* (2019). Mitophagy inhibits amyloid-beta and tau pathology
876 and reverses cognitive deficits in models of Alzheimer's disease. Nat Neurosci *22*, 401-412.

878 Foo, S.S., Chen, W., Chan, Y., Lee, W.S., Lee, S.A., Cheng, G., Nielsen-Saines, K., Brasil, P., and
879 Jung, J.U. (2018). Biomarkers and immunoprofiles associated with fetal abnormalities of ZIKV-
880 positive pregnancies. JCI Insight *3*, e124152.

882 Fujimaki, M., Saiki, S., Sasazawa, Y., Ishikawa, K.I., Imamichi, Y., Sumiyoshi, K., and Hattori, N.
883 (2018). Immunocytochemical Monitoring of PINK1/Parkin-Mediated Mitophagy in Cultured
884 Cells. Methods Mol Biol *1759*, 19-27.

886 Gal-Ben-Ari, S., Barrera, I., Ehrlich, M., and Rosenblum, K. (2018). PKR: A Kinase to Remember.
887 Front Mol Neurosci *11*, 480.

889 Gilfoy, F.D., and Mason, P.W. (2007). West Nile virus-induced interferon production is mediated
890 by the double-stranded RNA-dependent protein kinase PKR. J Virol *81*, 11148-11158.

892 Gorman, M.J., Caine, E.A., Zaitsev, K., Begley, M.C., Weger-Lucarelli, J., Uccellini, M.B., Tripathi,
893 S., Morrison, J., Yount, B.L., Dinnon, K.H., 3rd*, et al.* (2018). An Immunocompetent Mouse
894 Model of Zika Virus Infection. Cell Host Microbe *23*, 672-685 e676.

896 Grant, A., Ponia, S.S., Tripathi, S., Balasubramaniam, V., Miorin, L., Sourisseau, M., Schwarz,
897 M.C., Sanchez-Seco, M.P., Evans, M.J., Best, S.M.*, et al.* (2016). Zika Virus Targets Human STAT2
898 to Inhibit Type I Interferon Signaling. Cell Host Microbe *19*, 882-890.

900 Harper, J.W., Ordureau, A., and Heo, J.M. (2018). Building and decoding ubiquitin chains for
901 mitophagy. Nat Rev Mol Cell Biol *19*, 93-108.

903 He, X., Zhu, Y., Zhang, Y., Geng, Y., Gong, J., Geng, J., Zhang, P., Zhang, X., Liu, N., Peng, Y.*, et al.*
904 (2019). RNF34 functions in immunity and selective mitophagy by targeting MAVS for autophagic
905 degradation. EMBO J *38*, e100978.

907 Heo, J.M., Ordureau, A., Paulo, J.A., Rinehart, J., and Harper, J.W. (2015). The PINK1-PARKIN
908 Mitochondrial Ubiquitylation Pathway Drives a Program of OPTN/NDP52 Recruitment and TBK1
909 Activation to Promote Mitophagy. Mol Cell *60*, 7-20.

911 Hirota, T., Kunitoku, N., Sasayama, T., Marumoto, T., Zhang, D., Nitta, M., Hatakeyama, K., and
912 Saya, H. (2003). Aurora-A and an interacting activator, the LIM protein Ajuba, are required for
913 mitotic commitment in human cells. Cell *114*, 585-598.

915 Hou, S., Kumar, A., Xu, Z., Airo, A.M., Stryapunina, I., Wong, C.P., Branton, W., Tchesnokov, E.,
916 Gotte, M., Power, C.*, et al.* (2017). Zika Virus Hijacks Stress Granule Proteins and Modulates the
917 Host Stress Response. J Virol *91*, e00474-17.

919 Jia, H., Peng, H., and Hou, Z. (2020). Ajuba: An emerging signal transducer in oncogenesis.
920 Pharmacol Res *151*, 104546.

922 Kam, Y.W., Leite, J.A., Lum, F.M., Tan, J.J.L., Lee, B., Judice, C.C., Teixeira, D.A.T., Andreata-
923 Santos, R., Vinolo, M.A., Angerami, R.*, et al.* (2017). Specific Biomarkers Associated With
924 Neurological Complications and Congenital Central Nervous System Abnormalities From Zika
925 Virus-Infected Patients in Brazil. J Infect Dis *216*, 172-181.

927 Kashatus, D.F., Lim, K.H., Brady, D.C., Pershing, N.L., Cox, A.D., and Counter, C.M. (2011). RALA
928 and RALBP1 regulate mitochondrial fission at mitosis. Nat Cell Biol *13*, 1108-1115.

930 Khaminets, A., Heinrich, T., Mari, M., Grumati, P., Huebner, A.K., Akutsu, M., Liebmann, L.,
931 Stolz, A., Nietzsche, S., Koch, N.*, et al.* (2015). Regulation of endoplasmic reticulum turnover by
932 selective autophagy. Nature *522*, 354-358.

933

934 Kim, Y., Park, J., Kim, S., Kim, M., Kang, M.G., Kwak, C., Kang, M., Kim, B., Rhee, H.W., and Kim,
935 V.N. (2018). PKR Senses Nuclear and Mitochondrial Signals by Interacting with Endogenous
936 Double-Stranded RNAs. Mol Cell *71*, 1051-1063 e1056.

937

938 McEwen, E., Kedersha, N., Song, B., Scheuner, D., Gilks, N., Han, A., Chen, J.J., Anderson, P., and
939 Kaufman, R.J. (2005). Heme-regulated inhibitor kinase-mediated phosphorylation of eukaryotic
940 translation initiation factor 2 inhibits translation, induces stress granule formation, and
941 mediates survival upon arsenite exposure. J Biol Chem *280*, 16925-16933.

942

943 Melchjorsen, J., Sorensen, L.N., and Paludan, S.R. (2003). Expression and function of
944 chemokines during viral infections: from molecular mechanisms to in vivo function. J Leukoc
945 Biol *74*, 331-343.

946

947 Michlmayr, D., Andrade, P., Gonzalez, K., Balmaseda, A., and Harris, E. (2017). CD14(+)CD16(+)
948 monocytes are the main target of Zika virus infection in peripheral blood mononuclear cells in a
949 paediatric study in Nicaragua. Nat Microbiol *2*, 1462-1470.

950

951 Michlmayr, D., Kim, E.Y., Rahman, A.H., Raghunathan, R., Kim-Schulze, S., Che, Y., Kalayci, S.,
952 Gumus, Z.H., Kuan, G., Balmaseda, A.*, et al.* (2020). Comprehensive Immunoprofiling of
953 Pediatric Zika Reveals Key Role for Monocytes in the Acute Phase and No Effect of Prior Dengue
954 Virus Infection. Cell Rep *31*, 107569.

955

956 Mills, E.L., Kelly, B., and O'Neill, L.A.J. (2017). Mitochondria are the powerhouses of immunity.
957 Nat Immunol *18*, 488-498.

958

959 Miner, J.J., and Diamond, M.S. (2016). Mechanisms of restriction of viral neuroinvasion at the
960 blood-brain barrier. Curr Opin Immunol *38*, 18-23.

961

962 Moehlman, A.T., and Youle, R.J. (2020). Mitochondrial Quality Control and Restraining Innate
963 Immunity. Annu Rev Cell Dev Biol *36*, 265-289.

964

965 Mottis, A., Herzig, S., and Auwerx, J. (2019). Mitocellular communication: Shaping health and
966 disease. Science *366*, 827-832.

967

968 Naveca, F.G., Pontes, G.S., Chang, A.Y., Silva, G., Nascimento, V.A.D., Monteiro, D., Silva, M.S.D.,
969 Abdalla, L.F., Santos, J.H.A., Almeida, T.A.P.*, et al.* (2018). Analysis of the immunological
970 biomarker profile during acute Zika virus infection reveals the overexpression of CXCL10, a
971 chemokine linked to neuronal damage. Mem Inst Oswaldo Cruz *113*, e170542.

972

973 Ordureau, A., Sarraf, S.A., Duda, D.M., Heo, J.M., Jedrychowski, M.P., Sviderskiy, V.O.,
974 Olszewski, J.L., Koerber, J.T., Xie, T., Beausoleil, S.A.*, et al.* (2014). Quantitative proteomics
975 reveal a feedforward mechanism for mitochondrial PARKIN translocation and ubiquitin chain
976 synthesis. Mol Cell *56*, 360-375.

977

978 Pakos-Zebrucka, K., Koryga, I., Mnich, K., Ljujic, M., Samali, A., and Gorman, A.M. (2016). The
979 integrated stress response. EMBO Rep *17*, 1374-1395.

980

981 Pierson, T.C., and Diamond, M.S. (2020). The continued threat of emerging flaviviruses. Nat
982 Microbiol *5*, 796-812.

983

984 Rabouw, H.H., Langereis, M.A., Anand, A.A., Visser, L.J., de Groot, R.J., Walter, P., and van
985 Kuppeveld, F.J.M. (2019). Small molecule ISRIB suppresses the integrated stress response within
986 a defined window of activation. Proc Natl Acad Sci U S A *116*, 2097-2102.

987

988 Rasool, S., Soya, N., Truong, L., Croteau, N., Lukacs, G.L., and Trempe, J.F. (2018). PINK1
989 autophosphorylation is required for ubiquitin recognition. EMBO Rep *19*, e44981.

990

991 Ruff, E.F., Muretta, J.M., Thompson, A.R., Lake, E.W., Cyphers, S., Albanese, S.K., Hanson, S.M.,
992 Behr, J.M., Thomas, D.D., Chodera, J.D.*, et al.* (2018). A dynamic mechanism for allosteric
993 activation of Aurora kinase A by activation loop phosphorylation. Elife *7*, e32766.

994

995 Samuel, M.A., Whitby, K., Keller, B.C., Marri, A., Barchet, W., Williams, B.R., Silverman, R.H.,
996 Gale, M., Jr., and Diamond, M.S. (2006). PKR and RNase L contribute to protection against lethal
997 West Nile Virus infection by controlling early viral spread in the periphery and replication in
998 neurons. J Virol *80*, 7009-7019.

999

1000 Sekine, S., and Youle, R.J. (2018). PINK1 import regulation; a fine system to convey
1001 mitochondrial stress to the cytosol. BMC Biol *16*, 2.

1002

1003 Sliter, D.A., Martinez, J., Hao, L., Chen, X., Sun, N., Fischer, T.D., Burman, J.L., Li, Y., Zhang, Z.,
1004 Narendra, D.P.*, et al.* (2018). Parkin and PINK1 mitigate STING-induced inflammation. Nature
1005 *561*, 258-262.

1006

1007 Song, Y., Zhou, Y., and Zhou, X. (2020). The role of mitophagy in innate immune responses
1008 triggered by mitochondrial stress. Cell Commun Signal *18*, 186.

1009

1010 Sprung, M., Dikic, I., and Novak, I. (2018). Flow Cytometer Monitoring of Bnip3- and Bnip3L/Nix-
1011 Dependent Mitophagy. Methods Mol Biol *1759*, 105-110.

1012

1013 Stone, A.E.L., Green, R., Wilkins, C., Hemann, E.A., and Gale, M., Jr. (2019). RIG-I-like receptors
1014 direct inflammatory macrophage polarization against West Nile virus infection. Nat Commun
1015 *10*, 3649.

1016

1017 Suthar, M.S., Diamond, M.S., and Gale, M., Jr. (2013). West Nile virus infection and immunity.
1018 Nat Rev Microbiol *11*, 115-128.

1019

1020 Taylor, R.T., Lubick, K.J., Robertson, S.J., Broughton, J.P., Bloom, M.E., Bresnahan, W.A., and
1021 Best, S.M. (2011). TRIM79alpha, an interferon-stimulated gene product, restricts tick-borne
1022 encephalitis virus replication by degrading the viral RNA polymerase. Cell Host Microbe *10*, 185-
1023 196.

1025 Torii, S., Kasai, S., Yoshida, T., Yasumoto, K.I., and Shimizu, S. (2020). Mitochondrial E3 Ubiquitin
1026 Ligase Parkin: Relationships with Other Causal Proteins in Familial Parkinson's Disease and Its
1027 Substrate-Involved Mouse Experimental Models. Int J Mol Sci *21*, 1202.

1029 Tricou, V., Minh, N.N., Farrar, J., Tran, H.T., and Simmons, C.P. (2011). Kinetics of viremia and
1030 NS1 antigenemia are shaped by immune status and virus serotype in adults with dengue. PLoS
1031 Negl Trop Dis *5*, e1309.

1033 West, A.P., Khoury-Hanold, W., Staron, M., Tal, M.C., Pineda, C.M., Lang, S.M., Bestwick, M.,
1034 Duguay, B.A., Raimundo, N., MacDuff, D.A.*, et al.* (2015). Mitochondrial DNA stress primes the
1035 antiviral innate immune response. Nature *520*, 553-557.

1037 Xia, H., Luo, H., Shan, C., Muruato, A.E., Nunes, B.T.D., Medeiros, D.B.A., Zou, J., Xie, X., Giraldo,
1038 M.I., Vasconcelos, P.F.C.*, et al.* (2018). An evolutionary NS1 mutation enhances Zika virus
1039 evasion of host interferon induction. Nat Commun *9*, 414.

1041 Yang, K., Huang, R., Fujihira, H., Suzuki, T., and Yan, N. (2018). N-glycanase NGLY1 regulates
1042 mitochondrial homeostasis and inflammation through NRF1. J Exp Med *215*, 2600-2616.
1043 Youle, R.J. (2019). Mitochondria-Striking a balance between host and endosymbiont. Science
1044 *365*.

1046 Yu, C.Y., Chang, T.H., Liang, J.J., Chiang, R.L., Lee, Y.L., Liao, C.L., and Lin, Y.L. (2012). Dengue
1047 virus targets the adaptor protein MITA to subvert host innate immunity. PLoS Pathog *8*,
1048 e1002780.

1050 Zhang, L., Qin, Y., and Chen, M. (2018). Viral strategies for triggering and manipulating
1051 mitophagy. Autophagy *14*, 1665-1673.

1053 Zorba, A., Buosi, V., Kutter, S., Kern, N., Pontiggia, F., Cho, Y.J., and Kern, D. (2014). Molecular
1054 mechanism of Aurora A kinase autophosphorylation and its allosteric activation by TPX2. Elife *3*,
1055 e02667.

1056

1057

1058

1059

1060

1061   **Figures and Legends:**

1062

1063   **Figure 1: Ajuba negatively regulates MAVS expression. A.** IFNβ mRNA induction following

1064   ectopic expression of MAVS alone or together with Ajuba or LIMD1 in HEK293T cells. **B.** Protein

1065   expression from an experiment in A. **C.** Confocal images of FLAG-Ajuba in either mock infected

1066   or SenV-infected cells stained for total mitochondria using mitotracker (green) and Ajuba (red).

1067   DAPI counterstains the nuclei. **D.** The experiment in A. was repeated with cells treated with

1068   200nM bafilomycin A1 (BafA1) or 200nM epoxomicin (epox) for 6 h prior to cell lysis. **E.**

1069   Western blot of HeLa cells transfected with MAVS, WT Parkin, C431F Parkin or Ajuba. DNA was

1070   normalized using a GFP expressing control plasmid. Error bars represent mean±SD; *P<0.05,

1071   **P<0.01, ***P<0.001 by one-way ANOVA.

1072

1073   **Figure 2: Ajuba is regulated by PINK1-Parkin mediated degradation during mitophagy. A.**

1074   Western blot of HEK293T cells expressing FLAG-Ajuba and treated with 10μM CCCP for the

1075   times indicated followed by cellular fractionation. Viniculin and TIM44 are used as fractionation

1076   controls for cytosol and mitochondrial enrichment, respectively. **B.** Western blot of HEK293T

1077   cells expressing GFP or FLAG-Ajuba and treated with tunicamycin or oligomycin for 5 h at

1078   5μg/ml. **C.** Western blot of HEK293T cells expressing FLAG-Ajuba following treatment with CCCP

1079   or starvation in Earl's balanced salt solution (EBSS) for 6 h. Mfn1 and FAM134B are used as

1080   positive controls for mitophagy and bulk autophagy, respectively. **D.** HeLa cells engineered to

1081   express Parkin or knocked out for PINK1 were transfected with FLAG-Ajuba and treated with

1082   10μM CCCP for 6 h. Quantification of Ajuba and Mfn1 expression by densitometry for 3

1083   experiments is shown. **E.** Representative Seahorse analysis of oxygen consumption rate (OCR) in

1084   WT, Ajuba$^{-/-}$ or PINK1$^{-/-}$ MEFs following treatment with oligomycin (2μM), FCCP (2μM) or

1085   rotenone + Antimycin A (0.5μM each). **F.** Calculated OCR associated with mitochondrial

1086   functions from three independent experiments performed in triplicate (mean±SD); *P<0.05 by

1087   two-way ANOVA.

1088

1089 **Figure 3: Ajuba interacts with PINK1, and promotes PINK1 autophosphorylation and**

1090 **mitophagy. A.** Mean fluorescence intensity of WT or Ajuba$^{-/-}$ MEFs were labeled with

1091 mitotracker green (200nM). **B.** WT or Ajuba$^{-/-}$ MEFs were labeled with mitotracker green and

1092 mitotracker red (200nM), treated with 10μM CCCP for 16 h with or without BafA1, and

1093 analyzed by flow cytometry. **C.** Reciprocal IP of *E.coli*-expressed human PINK1 and Ajuba. **D.**

1094 Autophosphorylation of human PINK1 (300nM) in the presence of increasing concentrations of

1095 Ajuba (0-300nM). Total protein was normalized with bovine serum albumin. **E.** Quantification of

1096 pThr257/total PINK1. **F.** Confocal microscopy of HeLa cells transfected with a plasmid

1097 expressing HA-Ub, followed by treatment with 10μM CCCP for 2 h and stained for pSer65-Ub

1098 (green). Nuclei were counterstained with DAPI (blue). **G.** Quantification of pSer65-Ub puncta

1099 per cell in HeLa cells in E demonstrating that signals are specific to PINK1-Parkin mediated

1100 mitophagy. **H.** pSer65-Ub assay in HEK293T cells expressing GFP or Ajuba. **I.** Western blot for

1101 total pSer65-Ub in HEK293T cells expressing Ajuba and treated with 10μM CCCP for 2 h. Error

1102 bars represent mean±SD from 3-4 independent experiments; *P<0.05, **P<0.01, ***P<0.001

1103 by one-way ANOVA.

1104

1105 **Figure 4: Zika virus NS5 binds to Ajuba to suppress mitophagy. A.** pSer65-Ub assay in HEK293T

1106 cells infected with ZIKV for 48 h and then treated with or without 10μM CCCP for 2 h. Error bars

1107 represent mean±SD; ***P<0.001 by one-way ANOVA. **B.** IP of FLAG-Ajuba and ZIKV NS5-HA

1108 expressed in HEK293T cells. **C.** Confocal microscopy demonstrating cytosolic co-localization of

1109 FLAG-Ajuba (red) and ZIKV NS5-HA (greyscale). **D.** HEK293T cells were transfected with plasmids

1110 expressing FLAG-Ajuba, GFP-Parkin and either GFP or ZIKV NS5-HA. Cells were treated with

1111 10μM CCCP for the times indicated. Cells were fractionated into mitochondrial fractions

1112 (enriched for TIMM44) or cytosolic fractions (enriched for viniculin and calreticulin)

1113 demonstrating that CCCP-induced mitochondrial localization of Ajuba and Parkin is delayed in

1114 the presence of ZIKV-NS5. **E.** Confocal microscopy of Huh7 cells expressing single plasmids

1115 encoding Ajuba-FLAG, MAVS, or ZIKV NS5-HA. Only MAVS strongly colocalizes with

1116 mitochondria stained for TOM20 (greyscale). **F.** Confocal image of cells co-expressing MAVS and

1117 Ajuba demonstrating recruitment of Ajuba to MAVS-positive mitochondria and disruption of

1118   MAVS aggregates (arrow). **G.** Confocal image demonstrating that co-expression of ZIKV NS5 in

1119   cells also expressing MAVS and Ajuba suppresses Ajuba recruitment and maintains MAVS

1120   aggregates.

1121

1122   **Figure 5: ZIKV replication in mitophagy-deficient MEFs is associated with amplified**

1123   **chemokine expression, PKR phosphorylation, and release of mitochondrial dsRNA. A.-B.**

1124   RNAseq in 3 replicate cultures of WT, PINK1$^{-/-}$ or Ajuba$^{-/-}$ MEFs that were **A.** mock-infected, or **B.**

1125   infected with ZIKV with MOI 0.1 and harvested at 72 hpi. **C.** Chemokine and IFN gene expression

1126   changes (log2 fold change) in ZIKV-infected cells compared to mock-infected cells at 72 hpi. **D.**

1127   ZIKV growth curves in WT (black) and Ajuba$^{-/-}$ (blue) MEFs treated with isotype control (open

1128   symbols) or anti-IFNAR1 mAb (closed symbols). *P$\leqq$0.05 by Mann-Whitney test. **E.** ZIKV growth

1129   curves in WT (black) and PINK1$^{-/-}$ (pink) MEFs treated with isotype control (open symbols) or

1130   anti-IFNAR1 mAb (closed symbols). **F.** Transmission electron microscopy images of WT and

1131   Ajuba$^{-/-}$ MEF at 72 hpi with ZIKV. White arrowheads indicate mitochondria; yellow arrowheads

1132   indicate sites of virus replication. **G.** Western blot demonstrating that ZIKV infection increases

1133   expression levels of PKR, phospho-PKR and ATF4 in the absence of PINK1 or Ajuba. Basal levels

1134   of phospho-PKR and ATF4 are also increased in uninfected PINK1$^{-/-}$ and Ajuba$^{-/-}$ MEFs compared

1135   to WT MEFs. **H.** Quantification by densitometry of p-PKR/PKR ratio in ZIKV-infected MEFs from

1136   2 independent experiments. **I.** WT, PINK1$^{-/-}$ or Ajuba$^{-/-}$ MEFs were stained for mitochondria

1137   (TOM20, red) and dsRNA (J2, green) at 4 h post treatment with vehicle or CCCP. Staining

1138   intensity of dsRNA was quantified by image J software . ****P<0.001 by two-way ANOVA. **J.**

1139   Treatment of MEFs with ethidium bromide (EthBr) demonstrating loss of mitochondrial

1140   genome-encoded cytochrome B (cytochrome B) but not nuclear genome-encoded Mfn1. **K.**

1141   EthBr treatment suppresses PKR phosphorylation in ZIKV-infected MEFs.

1142

1143   **Figure 6: The ISR favors virus replication but is uncoupled from pro-inflammatory chemokine**

1144   **and cytokine expression dependent on PKR.** Primary human dermal fibroblasts were infected

1145   with ZIKV (MOI 1) and treated with 500nM ISRIB or C16 for 24h prior to harvest. Release of

1146   infectious virus was measured by plaque assay. Inhibition of **B.** eIF2α phosphorylation or **C.** PKR

1147   phosphorylation was verified by Western blotting. **D.** Chemokines and **E-F.** cytokines were

1148   measured by Bioplex multiplex assay in culture supernatants from uninfected cells or cells

1149   infected with ZIKV at 24, 48 and 72 hpi. Error bars represent mean±SD from two experiments

1150   performed in triplicate; *P<0.05, **P<0.01, ***P<0.001, ****P<0.0001 by one-way ANOVA.

1151

1152   **Figure 7: Pro-inflammatory chemokines are expressed earlier in ZIKV-infected Ajuba$^{-/-}$ mice**

1153   **associated with increased virus invasion of tissues.** WT and Ajuba$^{-/-}$ mice were treated with 2

1154   mg anti-IFNAR mAb one day prior to infection with 10^3 PFU ZIKV. **A.** Serum protein levels of the

1155   chemokines and cytokines measured by Bioplex multiplex assays. *P≦0.05 by one-way ANOVA.

1156   **B.** Virus titers at 3 and 5 dpi in serum and tissues measured by plaque forming units (PFU)/ml

1157   serum. Error bars represent mean±SD; *P<0.05, **P<0.01, ****P<0.0001 by Mann-Whitney

1158   test.

1159

1160   **Supplementary Figures and Legends:**

1161

1162   **Supplemental Figure 1: Ajuba negatively regulates MAVS expression. A.** Efficiency of mRNA

1163   depletion of *AJUBA* or *LIMD1* in A549 cells at 48 h post transfection with siRNAs targeting each

1164   gene. **B.** Titer of VSV at 24 hpi of cells from C. Error bars represent mean±SD from 2

1165   independent experiments performed in duplicate; *P<0.05, **P<0.01, ***P<0.001 by one-way

1166   ANOVA.

1167

1168   **Supplemental Figure 2: Design and verification of Ajuba$^{-/-}$ mice using CRISPR/Cas9-mediated**

1169   **gene editing. A.** Exon structure of the *Ajuba* gene. *Ajuba* Exon 1 was targeted by the gRNA

1170   sequence CCGGAGTCCGAGAGTCTCAACTT. **B.** Sequence verification of gene disruption in two

1171   lines of mice designated 8216A and 8258B. **C.** Summary of sequence modifications and **D.**

1172   Predicted potential ORF expression.

1173

1174   **Supplemental Figure 3. Ajuba is phosphorylated by PINK1. A.** Confocal microscopy of HEK293T

1175   cells expressing FLAG-Ajuba (red), PINK1-V5 (green) or both showing co-localization of the two

1176   proteins (yellow). Nuclei were counterstained with DAPI (blue). **B.** Predicted phosphorylation

1177   Ser/Thr sites in the pre-LIM region of Ajuba are associated with PINK1, TBK1,

1178   AKT/PKA/PKB/PKC, and CDK1. Therefore Ajuba was expressed alone or co-expressed with TBK1

1179   or PINK1 and run on SDS-PAGE. Two bands were excised for analysis by mass spectrometry. The

1180   upper band (B) was identified as highly phosphorylated Ajuba. **C.** Ajuba sequence with

1181   predicted phosphorylation sites indicated. The table summarizes the mass spectrometry data

1182   showing the spectral counts of basally expressed (Band A) and highly phosphorylated Ajuba

1183   (Band B). This analysis suggested that Ajuba is basally phosphorylated at S79 and S119. TBK1

1184   induced further phosphorylation at S47, S69, S104, S141, S133 and S166. PINK1 induced specific

1185   phosphorylation of Ajuba at S39, but also induced phosphorylation of the TBK1-dependent

1186   residues as summarized in the Venn diagram.

1187

1188   **Supplemental Figure 4. RNAseq and DEG expression in WT, PINK1$^{-/-}$ and Ajuba $^{-/-}$ MEFs. A.**

1189   Gene Ontology (GO) terms from IPA analysis demonstrating higher expression of interferon and

1190   inflammatory pathways in the absence of PINK1 or Ajuba, including the role of PKR in interferon

1191   induction and antiviral response. **B.** Log P value of chemokine expression shown in Figure 6E. **C.**

1192   Individual genes from the pathway designated as 'role of PKR (EIF2AK2) in interferon induction

1193   and antiviral response' demonstrating high expression in Ajuba$^{-/-}$ and PINK1$^{-/-}$ MEFs.

1194

1195   **Supplemental Figure 5. *Ajuba* mRNA expression in mouse tissues by RNAScope.** *Ajuba* mRNA

1196   staining (brown) was observed in **A.** keratinocytes and endothelial cells in the skin, **B.** Sertoli

1197   cells in the testes, **C.** hepatocytes (arrowheads) and endothelial cells in the liver, **D.** epithelial

1198   and endothelial cells in the lung, **E.** ependymal cells and **F.** neurons (black arrowheads) and

1199   endothelial cells (white arrowheads) in the CNS. Tissue sections were counterstained with

1200   hematoxylin.

1201

1202   **Supplemental Figure 6. Schematic representation of findings.** ZIKV virus suppresses PINK1-

1203   Parkin-dendent mitophagy through the actions of NS5 binding to and inhibiting mitochondrial

1204   recruitment of Ajuba. This results in mitochondrial RNA release and PKR activation and

1205   activation of the ISR to create a cellular environment that favors virus replication. However,

1206   PKR-dependent amplification of chemokines and specific cytokines central to the pro-

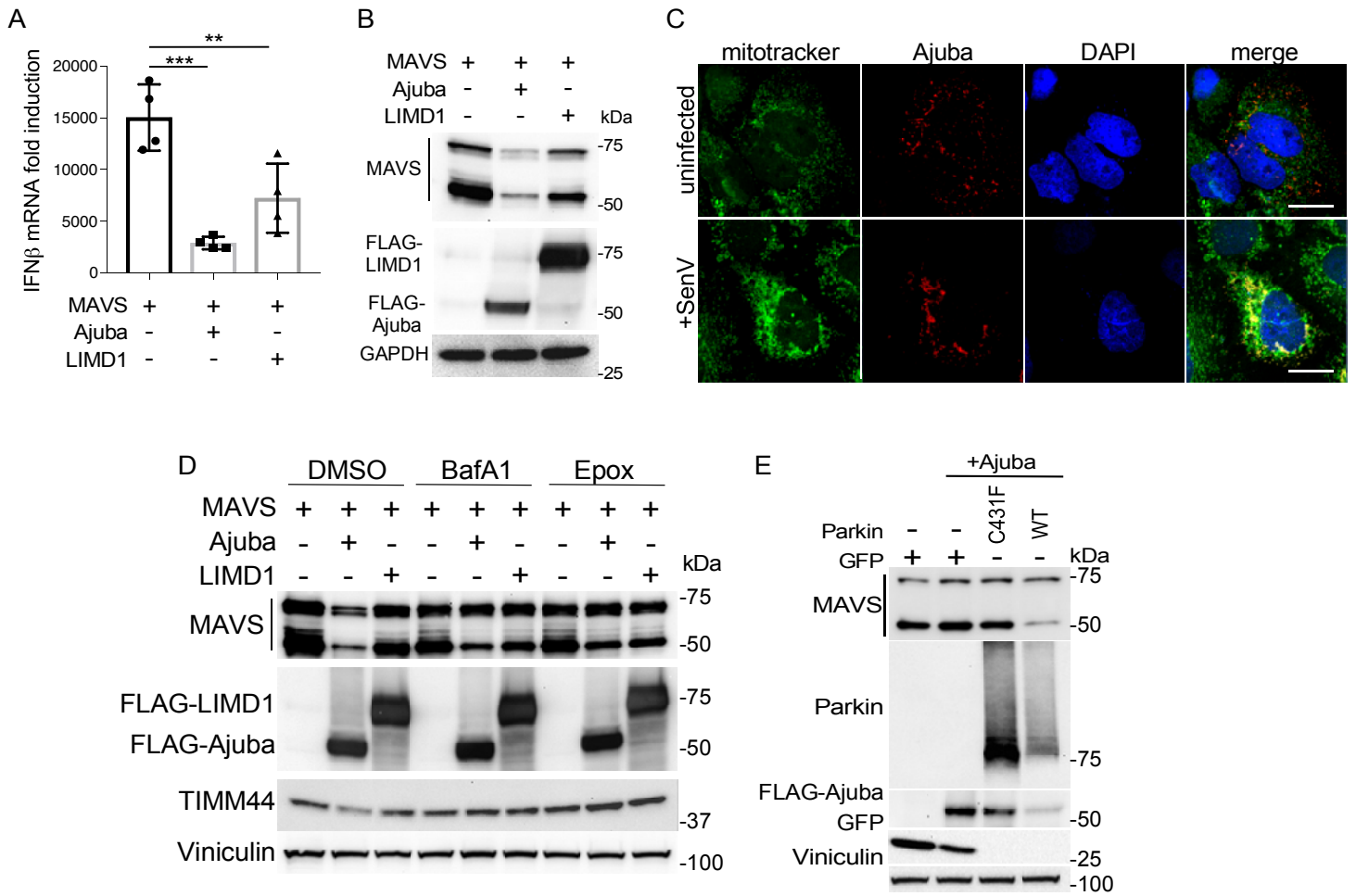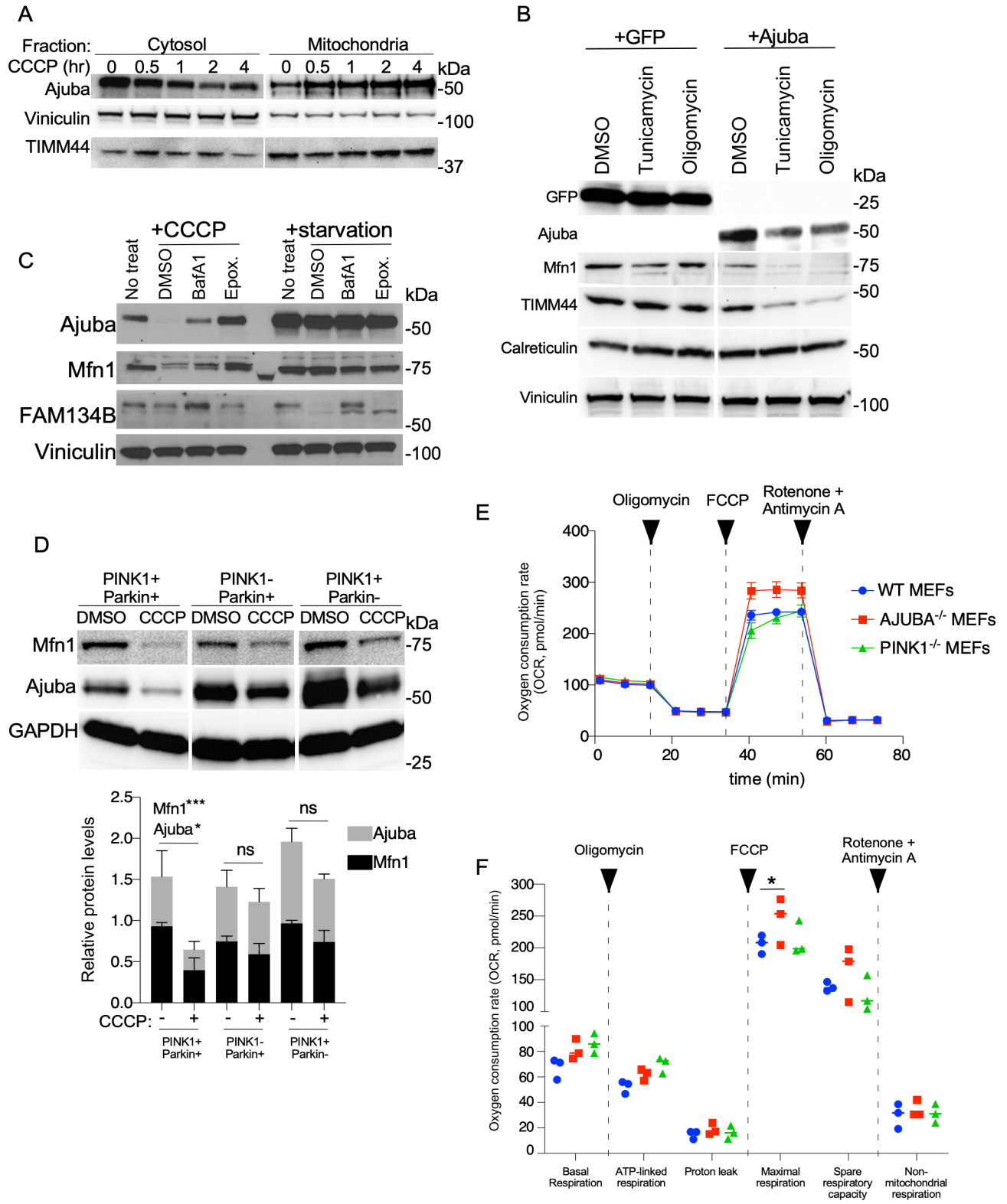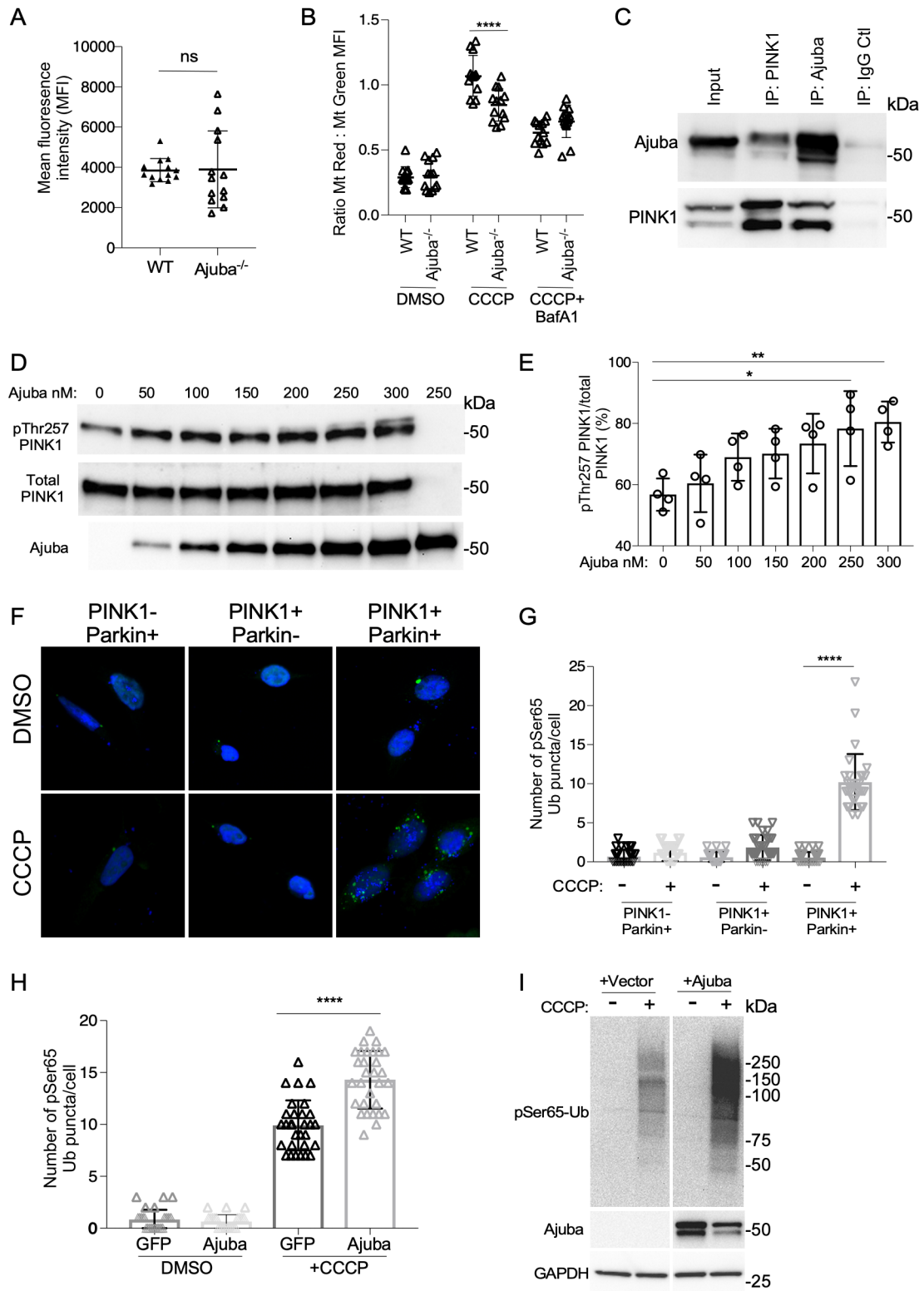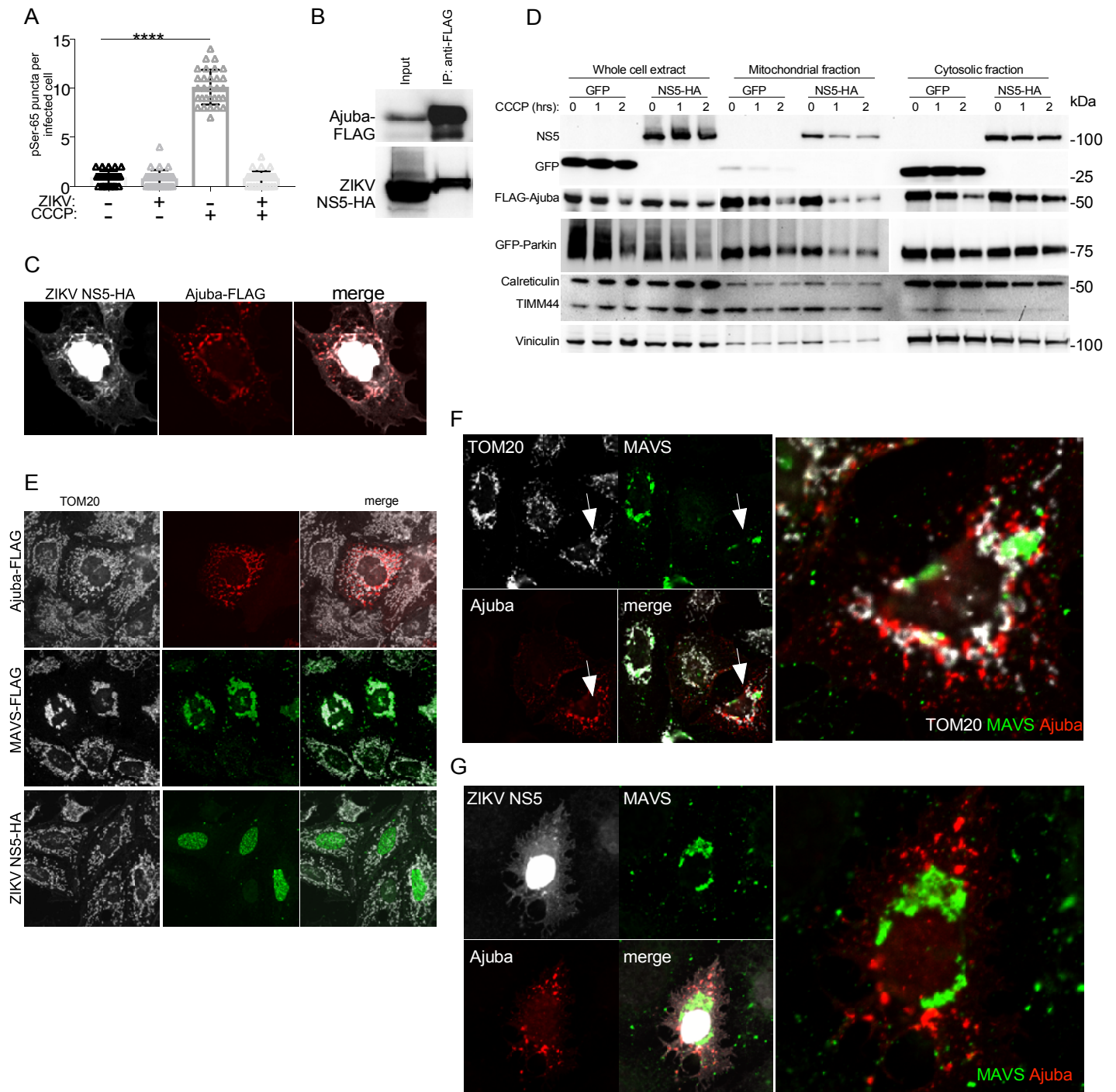1207   inflammatory response to ZIKV is uncoupled from virus replication.

A

B

C

D

E

Figure 1

Figure 2

Figure 3

Figure 4
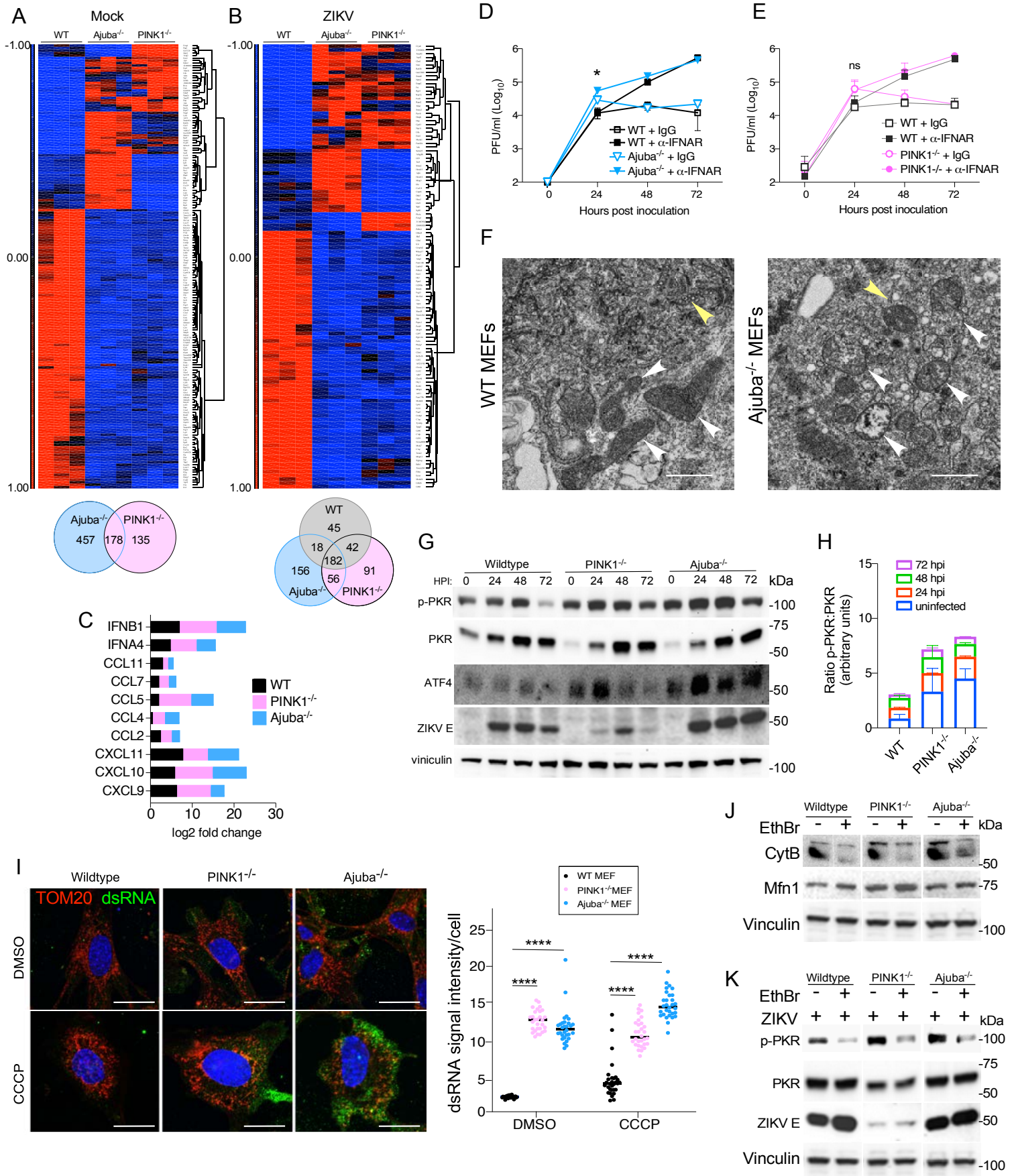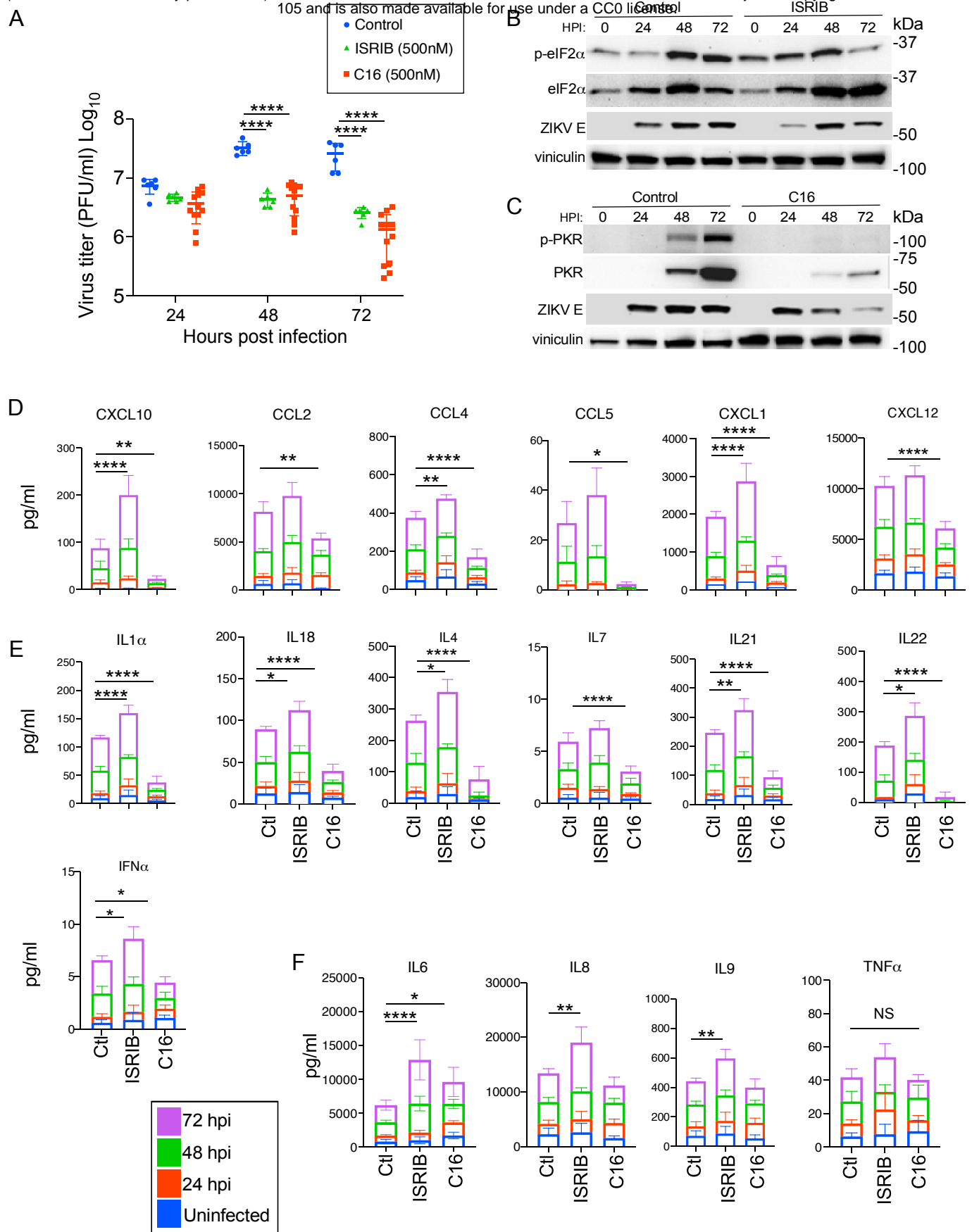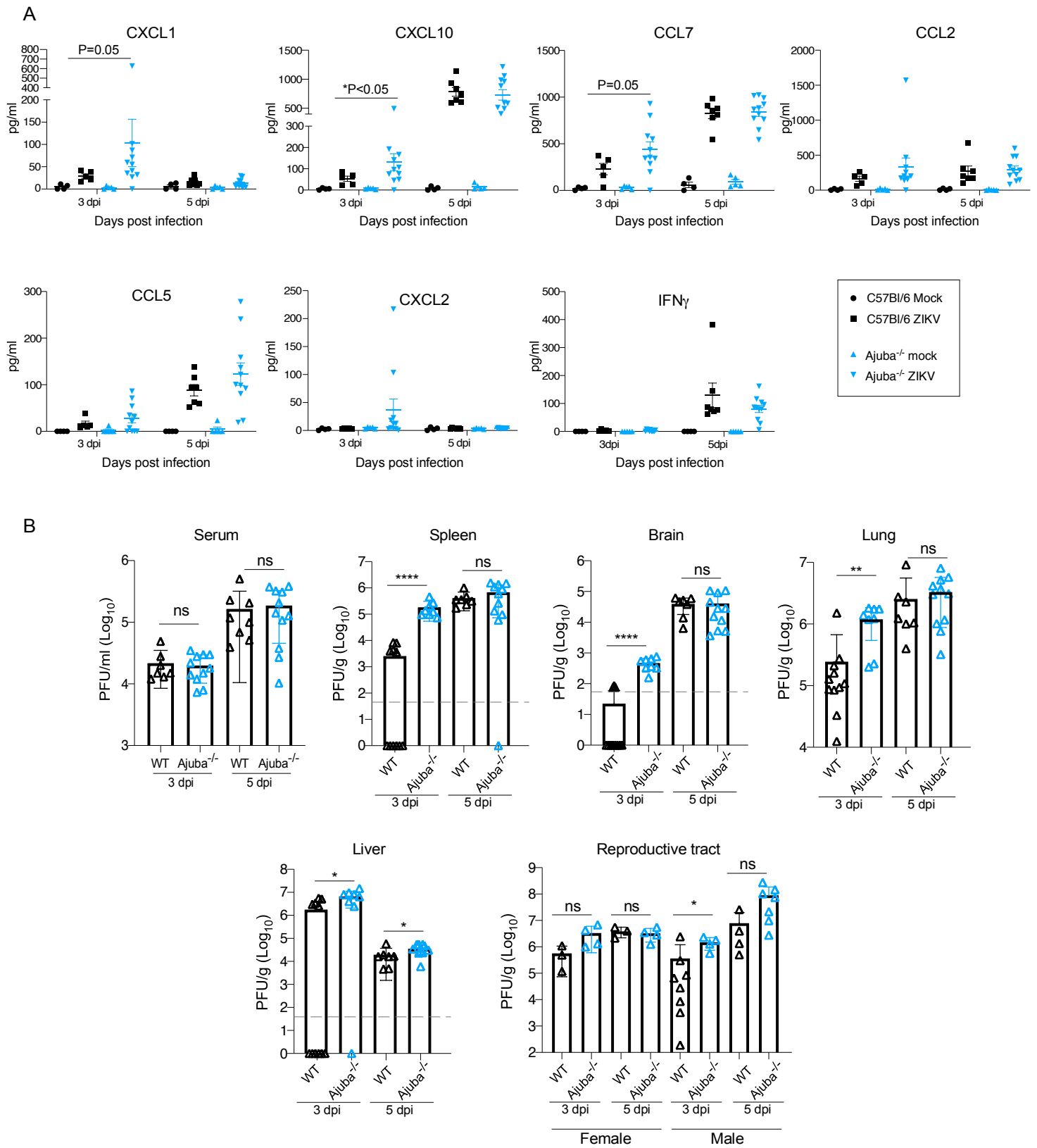
Figure 5

Figure 6

Figure 7

Supplementary Figure 1

A   CRISPR target site

B   Chromatograms and alignments

	PAM	Exon 1 Target Site
Reference	GCTTCGCCCTTTCTGCGGCCGAACTTGGCGCTG**CCG**GAGTCCGAGAGTCTCAACTTTTCT
Line 1	GCTTCGCCCTTTCTGCGGCCGAACTTGGCGCTGCCGGAG----AAGTCTCAACTTTTCT
Line 2	GCTTCGCCCTTTCTGCGGCCGA---------------------GAGTCTCAACTTTTCT

C   Mouse chromosome 14 mutation locations

Line#	Strain designation	Ajuba Exon 1 genotype
1	Ajuba$^{-/-}$8216A	4 nt deletion (54577209-54577212) and G-A SNP (54577214)
2	Ajuba$^{-/-}$8258B	22 nt deletion (54577192-54577213)

D   Predicted translations

Reference	548 aa
Line 1	372 aa
Line 2	372 aa

Supplementary Figure 2

A

| Ajuba-FLAG | PINK1-V5 | DAPI | merge |

Ajuba alone

PINK1 alone

PINK1+Ajuba
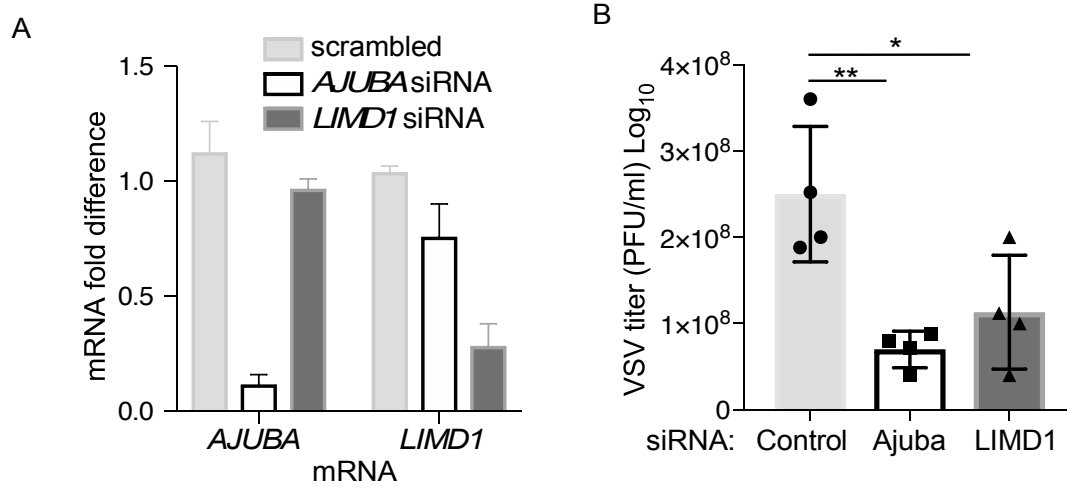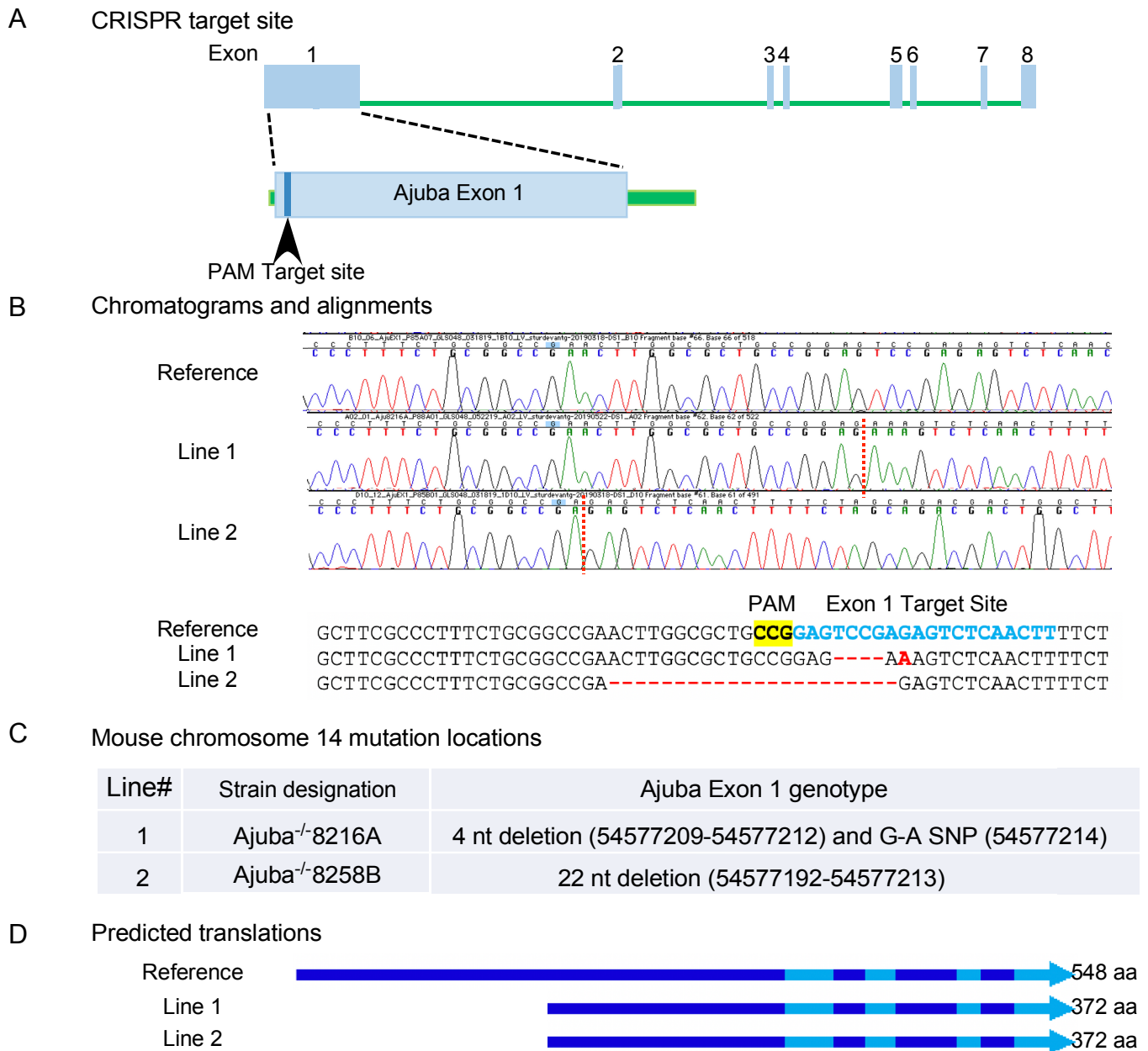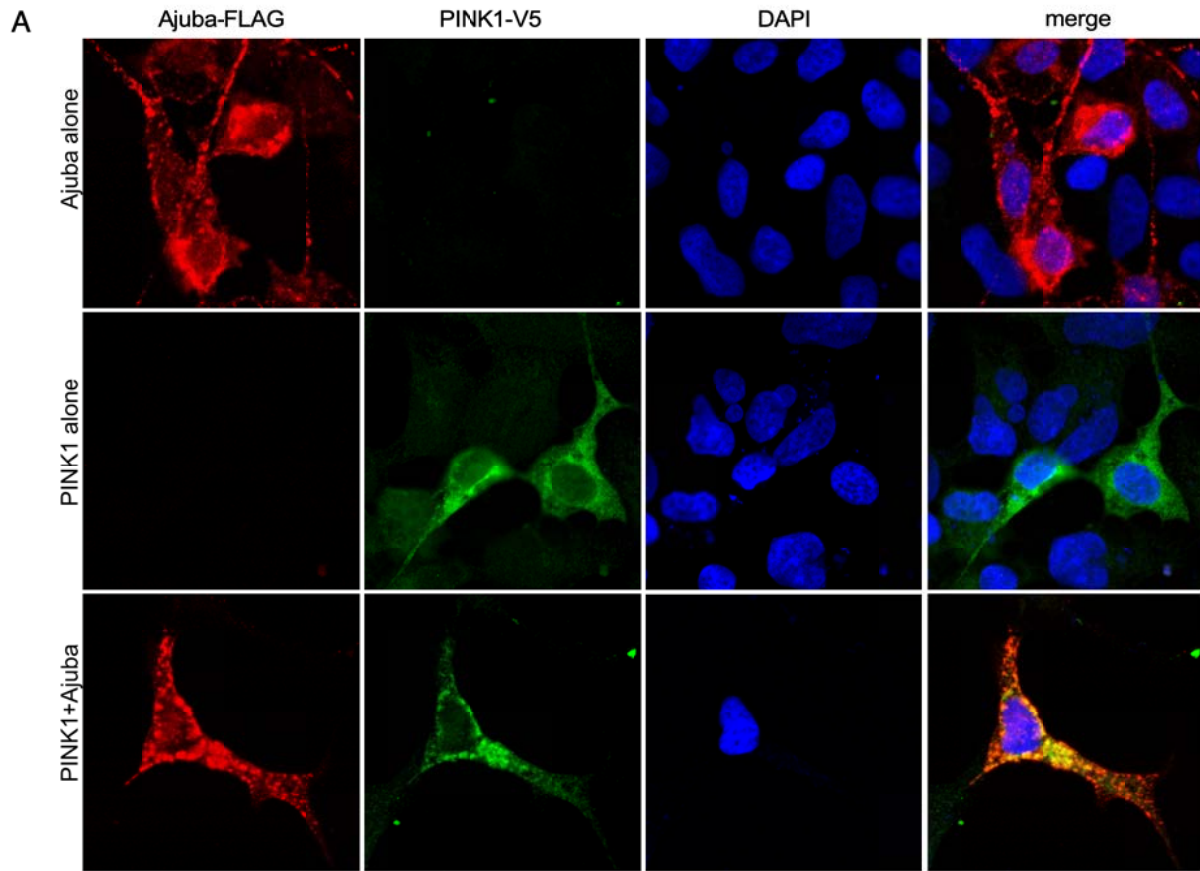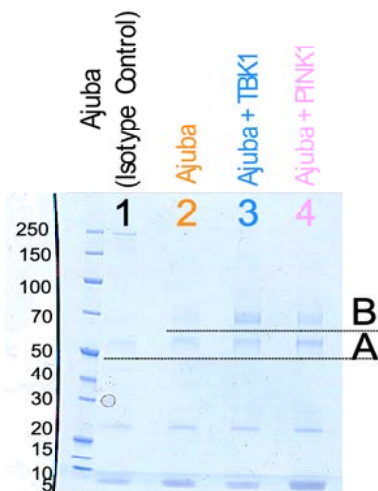
B

Predicted phosphorylation sites:

PINK1(S39/S136)
TBK1(S69/S104/S141)
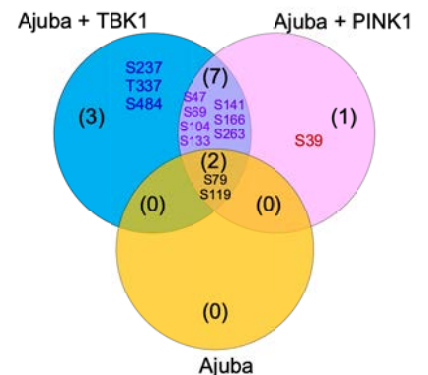AKT/PKA/PKB/PKC(S79)
CDK1 (S119, S175)

C

Mass spectometry data:

```
MERLGEKASR LLEKFGRRKG ESSRSGSDGT PGPGKGRLSG LGGPRKSGPR 50
GATGGPGDEP LEPAREQGSL DAERNQRGSF EAPRYEGSFP AGPPPTRALP 100
LPQSLPPDFR LEPTAPALSP RSSFASSSAS DASKPSSPRG SLLLDGAGAG 150
GAGGSRPCSN RTSGISMGYD QRHGSPLPAG PCLFGPPLAG AFAGYSPGGV 200
PSAYPELHAA LDRLYAQRPA GFGCQESRHS YPPALGSPGA LAGAGVGAAG 250
PLERRGAQPG RHSVTGYGDC AVGARYQDEL TALLRLTVGT GGREAGARGE 300
PSGIEPSGLE EPPGPFVPEA ARARMREPEA REDYFGTCIK CNKGIYGQSN 350
ACQALDSLYH TQCFVCCSCG RTLRCKAFYS VNGSVYCEED YLFSGFQEAA 400
EKCCVCGHLI LEKILQAMGK SYHPGCFRCI VCNKCLDGIP FTVDFSNQVY 450
CVTDYHKNYA PKCAACGQPI LPSEGCEDIV RVISMDRDYH FECYHCEDCR 500
MQLSDEEGCC CFPLDGHLLC HGCHMQRLNA RQPPANYI
```

Ajuba (Isotype Control)
Ajuba
Ajuba + TBK1
Ajuba + PINK1

| 1 | 2 | 3 | 4 |

250
150
100
70
50
40
30
20
15
10
5

B
A

Site	2A	2B	3A	3B	4A	4B
S39	0	0	0	0	0	2
S69	0	0	1	5	0	1
S104	0	0	1	3	0	1
S141	0	0	0	1	0	2
S79	0	3	0	3	0	1
S119	1	1	1	2	1	3
S166	0	0	2	4	0	1
S133	0	0	0	2	0	0
S47	0	0	0	1	0	1

AJUBA PHOSPHORYLATION

Ajuba + TBK1

Ajuba + PINK1

S237
T337
S484

(7)
S47 S141
S69 S166
S104 S263
S133

(3)

(1)
S39

(2)
S79
S119

(0)

(0)

(0)

Ajuba

Supplementary Figure 3

Supplementary Figure 4

Supplementary Figure 5